

## Late Quaternary slip rates across the central Tien Shan, Kyrgyzstan, central Asia

Stephen C. Thompson,<sup>1,2</sup> Ray J. Weldon,<sup>3</sup> Charles M. Rubin,<sup>4</sup> Kanatbek Abdrakhmatov,<sup>5</sup> Peter Molnar,<sup>6,7</sup> and Glenn W. Berger<sup>8</sup>

received 9 May 2001; revised 25 November 2001; accepted 30 November 2001; published 28 September 2002.

[1] Slip rates across active faults and folds show that late Quaternary faulting is distributed across the central Tien Shan, not concentrated at its margins. Nearly every intermontane basin contains Neogene and Quaternary syntectonic strata deformed by Holocene north-south shortening on thrust or reverse faults. In a region that spans two thirds of the north-south width of the central Tien Shan, slip rates on eight faults in five basins range from  $\sim 0.1$  to  $\sim 3$  mm/yr. Fault slip rates are derived from faulted and folded river terraces and from trenches. Radiocarbon, optically stimulated luminescence, and thermoluminescence ages limit ages of terraces and aid in their regional correlation. Monte Carlo simulations that sample from normally distributed and discrete probability distributions for each variable in the slip rate calculations generate most likely slip rate values and 95% confidence limits. Faults in basins appear to merge at relatively shallow depths with crustal-scale ramps that underlie mountain ranges composed of pre-Cenozoic rocks. The sum and overall pattern of late Quaternary rates of shortening are similar to current rates of north-south shortening measured using Global Positioning System geodesy. This similarity suggests that deformation is concentrated along major fault zones near range-basin margins. Such faults, separated by rigid blocks, accommodate most of the shortening in the upper crust.

*INDEX TERMS:* 8107 Tectonophysics: Continental neotectonics; 9320 Information Related to Geographic Region: Asia; 8010 Structural Geology: Fractures and faults;

*KEYWORDS:* Tien Shan, fault-related folding, slip rates, Quaternary, river terrace, Kyrgyzstan

**Citation:** Thompson, S. C., R. J. Weldon, C. M. Rubin, K. Abdrakhmatov, P. Molnar, and G. W. Berger, Late Quaternary slip rates across the central Tien Shan, Kyrgyzstan, central Asia, *J. Geophys. Res.*, 107(B9), 2203, doi:10.1029/2001JB000596, 2002.

### 1. Introduction

[2] Different ideas, if not theories, of mountain building anticipate different spatial and temporal partitioning of strain during the growth of mountain belts. Many convergent belts, particularly in plate boundary settings, have a dominant vergence and also show a unidirectional propagation of major faults that incorporate material by frontal accretion [Bally *et al.*, 1986; Butler, 1986; Dahlstrom, 1970; Le Fort, 1975; Mattauer, 1975]. These characteristics

are generally associated with simple shear on a gently dipping fault that underlies the belt [Cook *et al.*, 1979; Mugnier *et al.*, 1990; Nelson *et al.*, 1996], a boundary condition suitable for critical wedge theory [Dahlen, 1984; Davis *et al.*, 1983; Willett, 1992]. At first, the shortening rates across these thrust belts were believed to be localized at a frontal fault [e.g., Boyer and Elliott, 1982; Dahlstrom, 1970], and field studies show that this condition does exist in nature, at least at one prominent belt [Lavé and Avouac, 2000]. Geologic [e.g., Boyer, 1992], analog [e.g., Koyi *et al.*, 2000], and numerical [Willett, 1999] studies, however, show that strain rates cannot only be concentrated at a frontal fault but also distributed across the entire deforming orogen.

[3] Other convergent mountain belts, commonly called “thick-skinned” and often formed far from plate boundaries, lack a dominant direction of vergence, tend to contain widely spaced, fault-bounded ranges and basins, and lack clear association with an underlying low-angle fault [Gries, 1983; Jordan and Allmendinger, 1986; Molnar and Tapponnier, 1975; Rodgers, 1987; Tapponnier and Molnar, 1979]. Although Earth scientists have long recognized differences among convergent mountain belts, inferences about the partitioning of strain rate across thick-skinned belts have been based on geological and geophysical observations with mostly qualitative results.

<sup>1</sup>Department of Geological Sciences, University of Washington, Seattle, Washington, USA.

<sup>2</sup>Now at Department of Geological Sciences, University of Oregon, Eugene, Oregon, USA.

<sup>3</sup>Department of Geological Sciences, University of Oregon, Eugene, Oregon, USA.

<sup>4</sup>Department of Geological Sciences, Central Washington University, Ellensburg, Washington, USA.

<sup>5</sup>Kyrgyz Institute of Seismology, Academy of Science, Bishkek, Kyrgyzstan.

<sup>6</sup>Department of Earth, Atmosphere, and Planetary Sciences, Massachusetts Institute of Technology, Cambridge, Massachusetts, USA.

<sup>7</sup>Now at Department of Geological Sciences and CIRES, University of Colorado, Boulder, Colorado, USA.

<sup>8</sup>Desert Research Institute, Reno, Nevada, USA.

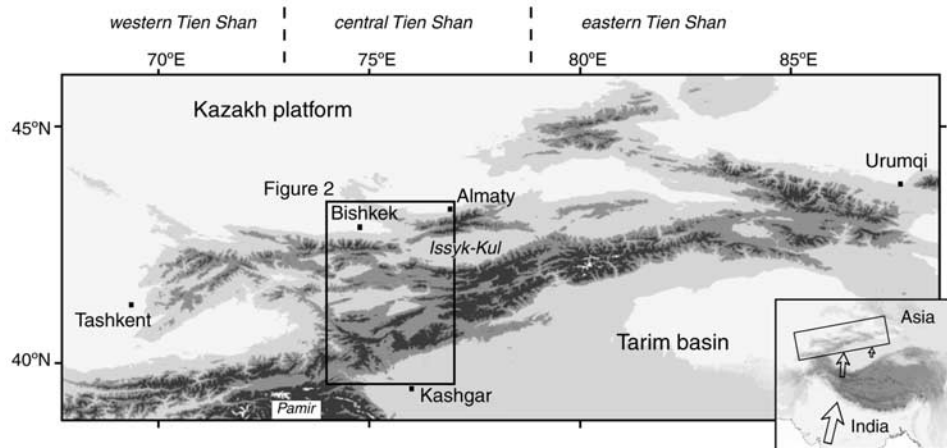


**Figure 1.** Map of the Tien Shan, with shades of gray indicating 1000-, 2500-, 3500-, and 5500-m elevation contours. Approximate boundaries between the western, central, and eastern Tien Shan indicated at the top of the map. Inset map shows the location of the Tien Shan in central Asia; the arrows show the motion of the Indian Plate and the Tarim basin relative to the Eurasian Plate.

[4] The thick-skinned Tien Shan of central Asia, a product of India-Eurasia plate convergence, exemplifies late Cenozoic mountain building by distributed deformation [e.g., Burbank *et al.*, 1999; Cobbold *et al.*, 1994; Makarov, 1977; Sadybakasov, 1972, 1990; Schulz, 1948; Tapponnier and Molnar, 1979]. Global Positioning System (GPS) measurements indicate that  $\sim 12$ – $13$  mm/yr north-south shortening rate is broadly distributed across the northern two thirds of the central Tien Shan [Abdrakhmatov *et al.*, 1996]. Most investigations of active tectonics in the Tien Shan thus far have focused on the timing and rates of slip on thrust fault systems that bound the northern and southern margins [Avouac *et al.*, 1993; Brown *et al.*, 1998; Burchfiel *et al.*, 1999; Yin *et al.*, 1998]. The partitioning of late Quaternary geologic shortening among faults in the interior and at the margins of the belt has not been quantified.

[5] We ask how geologic strain rates are distributed across the central Tien Shan. Do faults on the margins of the mountain belt accommodate a higher proportion of the total strain rate than faults of the interior? Does slip on major faults account for all or most of the total strain rate, or is a large portion of upper crustal strain accommodated by penetrative deformation away from major faults? We present measurements of late Quaternary rates of slip on faults across the width of the Kyrgyz central Tien Shan, a region that spans the northern two thirds of the belt. We use river terraces and alluvial fans as strain markers. The compilation of slip rates provides a snapshot of geologic deformation within a short time interval ( $\sim 150,000$  years). We find a similar rate and pattern of north-south shortening between geologic and geodetic measurements, indicating that a few faults, spread across the belt, are responsible for most deformation in the upper crust.

## 2. Tectonic and Geologic Setting

[6] The central and eastern Tien Shan forms an elongate deforming region between two generally stable crustal elements: the Kazakh platform to the north and the Tarim

basin to the south (Figure 1). Though  $\sim 1000$ – $1500$  km north of the Indo-Eurasian plate boundary, the central Tien Shan presently absorbs nearly one-half of the total relative plate convergence of  $\sim 45$  mm/yr [Abdrakhmatov *et al.*, 1996; DeMets *et al.*, 1994; Holt *et al.*, 2000]. Focal mechanisms from moderate and large earthquakes show primarily thrust and reverse faulting with  $P$  axes oriented approximately north-south, consistent with the geodetically measured maximum shortening direction and the overall direction of Indo-Eurasian plate convergence [Ghose *et al.*, 1998; Nelson *et al.*, 1987; Ni, 1978; Shirokova, 1974; Tapponnier and Molnar, 1979].

[7] The central Tien Shan displays a basin-and-range topography with late Cenozoic relief caused by distributed reverse faulting and folding [Chediya, 1986; Makarov, 1977; Sadybakasov, 1972, 1990; Schulz, 1948; Tapponnier and Molnar, 1979] (Figures 1 and 2). The generally east-west trending ranges of the central Tien Shan define blocks composed of previously deformed Paleozoic rocks [e.g., Burtman, 1975; Knauf, 1976] and separate basins of syn-tectonic Cenozoic deposits.

[8] Basins in the central Tien Shan share general similarities in active fault location, length, orientation, and sense of displacement (Figure 2). Holocene and late Pleistocene thrust faults commonly lie within the basin interiors, kilometers or tens of kilometers from faults and folds that mark the range-basin margins. The hanging walls of faults within the basins have deformed strata from shallow flat-and-ramp-style thrust faulting. Narrow bands of hills within the basins overlie active thrust ramps. The fault geometry implies a transfer of displacement at depth from a steep crustal ramp that underlies the basin margin to a shallow fault that extends into the basin [Ikeda, 1983]. This kinematic relationship is common in the Tien Shan [Avouac *et al.*, 1993; Brown *et al.*, 1998; Burchfiel *et al.*, 1999; Molnar *et al.*, 1994] and other convergent orogens [Benedetti *et al.*, 2000; Gries, 1983; Ikeda, 1983; Yeats and Lillie, 1991].

[9] Holocene and late Pleistocene fault traces are discontinuous, with alternating buried and exposed fault tip

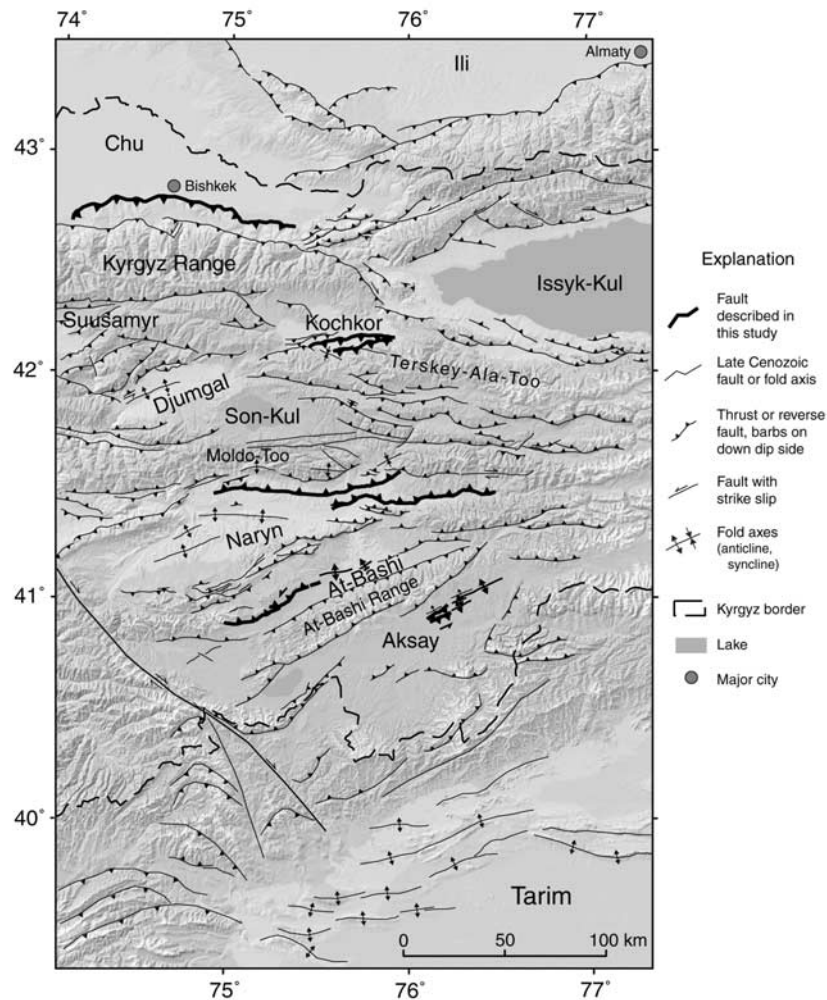


**Figure 2.** Active faults and folds in the central Tien Shan. Major intermontane basins and lakes and selected ranges are labeled. Thick lines are faults and folds for which we have determined late Quaternary slip rates. The fault and fold traces were compiled from satellite and air photo interpretation, field observations, and previous studies.

lines, and many fault lengths are shorter than the basins and ranges they occupy or bound (Figure 2). Most faults strike east-west to east-northeast, following the ancient structural grain of Paleozoic rocks in the ranges. Although several faults show evidence for dextral or sinistral components of motion, as revealed by exposed fault plane striae or laterally deflected landforms [Abdrakhmatov *et al.*, 2001a; Cobbold *et al.*, 1994; Makarov, 1977], most of the late Quaternary faults indicate dominantly dip-slip motion. The right-lateral strike-slip Talas-Ferghana fault [Burtman, 1964; Burtman *et al.*, 1996; Trifonov *et al.*, 1991], lying west of our study area, is a notable exception.

### 3. River Terraces

[10] Terraces occur along many river valleys that cross the margins of intermontane basins in the Kyrgyz Tien Shan. A terrace forms when a river incises its floodplain and transport of material by the river ceases on the terrace tread. If incision occurs rapidly, the river terrace represents a time line with a shape that is approximately planar over distances of several hundred meters [cf. Weldon, 1986].

Because they represent potentially datable surfaces, river terraces that cross active faults and folds make ideal strain markers for the study of rates and kinematics of deformation [Avouac *et al.*, 1993; Lavé and Avouac, 2000; Molnar *et al.*, 1994; Rockwell *et al.*, 1988; Weldon and Sieh, 1985].

[11] River terraces within and between intermontane basins in the Kyrgyz Tien Shan have been correlated based on morphology [Grigorienco, 1970; Makarov, 1977]. The regional terrace sequence consists of four main divisions (QI, QII, QIII, and QIV) originally associated with early, middle, and late Pleistocene and Holocene ages. Major terrace divisions contain one to several subdivisions, which we define in parentheses, e.g., QII(2). Like the major divisions, younger subdivisions within each main division have greater numbers. Although the exact number of terraces within each division can vary locally, certain prominent terraces recur from basin to basin and drainage to drainage. Radiocarbon, thermoluminescence (TL), and infrared-stimulated luminescence (IRSL) ages collected thus far support the correlation of the prominent QIII(2) and QII(2) terraces.

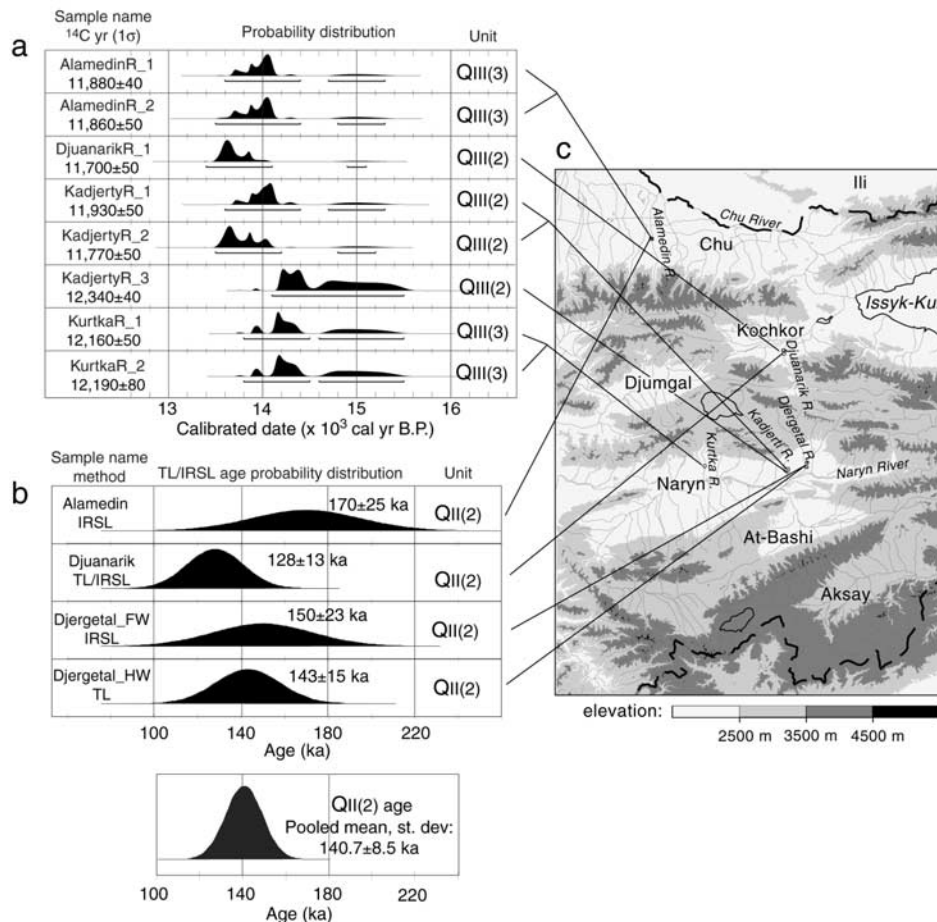


**Figure 3.** (a) Radiocarbon calibrated age probability distributions for eight detrital charcoal samples collected from the QIII(2) and QIII(3) river terraces (Table 1). The similar calibrated age ranges suggest that river incision and river terrace formation occurred during a short time interval around  $13.5\text{--}15.7 \times 10^3$  calibrated years before present (cal years B.P.) in several intermontane basins. Calibration plots generated by Oxcal version 3.5 [Ramsey, 1995] with the calibration data of Stuiver et al. [1998]; horizontal bars beneath distributions indicate 95% confidence intervals. (b) TL and IRSL age distributions ( $1\sigma$  shown) of silt collected from fine-grained sediments covering QII(2) terraces (Table 2). The Djergetal River samples were collected from terrace treads correlated across a fault, and are  $\sim 5$  km apart. The pooled mean age and standard distribution (square root of variance) of the four ages is shown below, and we use this distribution for the age of the QII(2) terrace. (c) Index map of the central Tien Shan; extent similar to Figure 2.

[12] Calibrated radiocarbon ages of detrital charcoal limit the timing of formation of the broad, paired QIII(2) terrace and immediately inset QIII(3) terrace in four drainage basins and three intermontane basins (Figure 3 and Table 1). The typical stratigraphy beneath a terrace tread includes a bedrock strath (most commonly formed on weakly cemented Tertiary sandstone and siltstone), a few meters of cobble gravel, and a few centimeters to several meters of fine-grained silt and sand that we interpret as overbank deposits, colluvium, or loess. If the contact between gravel and fine-grained sediment represents floodplain abandonment and river incision, then the first sediments deposited above the contact closely date or postdate the terrace formation [Lavé and Avouac, 2000; Merritts et al., 1994]. Seven detrital charcoal samples were collected from the lower portions of fine-grained sediments overlying river gravel; only one sample was collected from within fluvial gravel (Table 1).

Thus most samples represent minimum limiting ages for the river terrace formation. Detrital charcoal, however, predates the deposit from which it was collected because of a nonzero inherited age (a combination of an age of the plant and age of sediment reworking).

[13] The calibrated age distributions of charcoal samples collected close to the QIII(2) and QIII(3) terrace gravel contacts overlap, with  $\sim 98\%$  of the probability distribution between  $13.5$  and  $15.7 \times 10^3$  cal years B.P. (Figure 3 and Table 1). This result suggests that the radiocarbon ages sample the same event, even though they came from terraces in different drainage basins. Other factors, such as the time between incision of the QIII(2) and the QIII(3) terraces, the time of initial aggradation of fine-grained material after formation of the terraces, and the inherited age of charcoal fragments, appear small compared to the uncertainty in the age distribution. The similar calibrated radiocarbon ages

**Table 1.** Radiocarbon Ages and Calibration of Charcoal Samples

Sample Code	Laboratory <sup>a</sup>	Age, <sup>b,c,d</sup> <sup>14</sup> C years B.P.(±1 σ)	Age Range at 95% Confidence, <sup>c</sup> cal years B.P.	Area <sup>f</sup>	Sample Location	Terrace Level or Stratigraphic Unit <sup>g</sup>	Height Above Gravel Contact, <sup>h</sup> m
SCT/090899/8(4)	59758	11,880 ± 40	13,620–14,100 14,230–14,260 14,780–14,830	0.978 0.011 0.011	Alamedin River; Chu basin	QIII(3)	+0.50
SCT/090899/8(5)	59760	11,860 ± 50	13,550–14,100 14,230–14,260	0.993 0.007	Alamedin River; Chu basin	QIII(3)	+0.50
99/Koch/2e	57622	11,700 ± 50	13,450–13,900 13,940–13,960	0.996 0.004	Djuanarik River; Kochkor basin	QIII(2)	+1.10
99/Kurtka/5	57606	12,160 ± 50	13,830–13,950 14,050–14,370 14,620–15,340	0.094 0.521 0.385	Kurtka River; Naryn basin	QIII(3)	+0.10
99/Kurtka/10	57607	12,190 ± 80	13,830–13,950 14,040–14,390 14,600–15,380	0.077 0.502 0.421	Kurtka River; Naryn basin	QIII(3)	+0.15
98/Kadj/1	51037	11,930 ± 50	13,640–14,110 14,220–14,260	0.982 0.018	Kadjerty River; Naryn basin	QIII(2); (terrace tread)	+0.30
98/Kadj/2	51038	11,770 ± 50	13,490–14,020	1.000	Kadjerty River; Naryn basin	QIII(2); (terrace tread)	+0.10
98/KadjQ3tr/11	51036	12,340 ± 40	14,110–14,440 14,540–15,430	0.433 0.567	Kadjerty River; Naryn basin	QIII(2); (Fault scarp)	–0.10
98/Odjar/100	51044	8180 ± 50	9010–9290	1.000	Oinak-Djar; At-Bashi basin	layer A; (trench site)	(+0.05)
98/Odjar/8	51039	8790 ± 40	9600–9940 9990–10,150	0.913 0.087	Oinak-Djar; At-Bashi basin	layer C; (trench site)	(+0.25)
99/Odjar/104	51040	9140 ± 50	10,210–10,420 10,460–10,470	0.983 0.017	Oinak-Djar; At-Bashi basin	layer C; (trench site)	(+0.20)

<sup>a</sup> Samples prepared and run at Center for Accelerator Mass Spectrometry, Lawrence Livermore National Laboratories.

<sup>b</sup> Delta <sup>13</sup>C values of –25‰ are assumed according to *Stuiver and Polach* [1977].

<sup>c</sup> The quoted age is in radiocarbon years using the Libby half-life of 5568 years and following the conventions of *Stuiver and Polach* [1977].

<sup>d</sup> Sample preparation backgrounds have been subtracted, based on measurements of samples of <sup>14</sup>C-free coal. Backgrounds were scaled relative to sample size.

<sup>e</sup> Calibration with CALIB [*Stuiver and Reimer*, 1986] version 4.3 using calibration data of *Stuiver et al.* [1998].

<sup>f</sup> Relative area under the probability distribution that lies within the 95% confidence limits.

<sup>g</sup> Entries in parentheses are site names.

<sup>h</sup> Values in parentheses indicate height above lower contact of unit.

indicate that widespread river incision and terrace formation occurred during the most recent global glacial-to-interglacial transition [*Fairbanks*, 1989; *Imbrie et al.*, 1984].

[14] Silt overlying river gravel was collected for TL and IRSL dating from four older terraces mapped as QII(2) along three drainages in different intermontane basins (Figure 3 and Table 2). For a TL or IRSL age to represent the time of deposition, the silt grains within an unheated sample must be sufficiently “bleached” by sunlight so as to empty light-sensitive electron traps [*Aitken*, 1985, 1998]. All the samples consist of silt to sandy silt from deposits 2–30 m thick that overlie fluvial gravel and are interpreted to be a combination of flood overbank deposits, loess, and minor colluvium.

[15] The four TL and IRSL ages are not statistically different at the 95% confidence interval and have a pooled mean age and standard deviation (1σ) of 140.7 ± 8.5 ka (Figure 3 and Appendix C). In slip rate calculations we use this result as the age of the QII(2) terrace. We further infer that the terrace formed during the penultimate global glacial-to-interglacial transition, ~128–140 ka [*Henderson and Slowey*, 2000; *Imbrie et al.*, 1984; *Shackleton*, 2000].

[16] Because most of our radiocarbon samples and all of our TL and IRSL samples are derived from fine-grained material that overlies river gravel of the terraces, most of our ages represent minimum ages of paleoriver incision. Nevertheless, because of the close agreement between ages of

terraces in different drainage basins we infer that (1) paleoriver incision occurred rapidly along the reaches that cross the active faults, (2) deposition of sediments (and datable material) overlying river gravel occurred rapidly after river incision, and (3) the ages reflect the timing of sediment deposition (e.g., minimal inherited age of charcoal; complete resetting of electron traps in silt), at least within the range of measurement uncertainties [*Thompson*, 2001]. Furthermore, the data are consistent with the hypothesis that the hydrologic changes that caused the paleoriver incision and terrace formation coincided with major changes in global climate, even though paleoclimate in continental interiors need not correlate with global climate proxies, such as sea level change [*Gillespie and Molnar*, 1995].

[17] We surveyed river terrace treads and fault scarps with a laser distance theodolite (total station) and differential Global Positioning System receivers. Uncertainties in relative positions made with these instruments are less than a few decimeters and are less than the local variability in the position of the geologic contacts or geomorphic surfaces that we measured. For river terraces covered with thick or variable deposits of loess or colluvium, we surveyed the contact between fluvial gravel and overlying fine-grained deposits. This contact surpasses the strath as a strain marker for two reasons. First, in several locations we observed variability in the thickness of the river gravel overlying the strath that corresponded to changes in the local vertical component of slip [see also *Molnar et al.*, 1994]. This

**Table 2.** TL and IRSL Data and Ages of QII(2) Terraces

Sample Code <sup>a,b</sup>	Laboratory <sup>a,b</sup>	Dose Rate <sup>c</sup> $D_R \pm 1\sigma$ , Gyr/kyr	Mode	Preheat <sup>d</sup>	Bleach <sup>e</sup>	Equivalent Dose <sup>f</sup> $D_E \pm 1\sigma$ , Gyr	Time <sup>g</sup> , s	Temp <sup>g</sup> , °C	Age <sup>h</sup> $\pm 1\sigma$ , kyr	Sample Location	Material	Thickness of Deposit, m	Height Above Gravel, m
SCT/090899	TIEN99-1	$5.55 \pm 0.60$	IRSL	160°C/2 d	780/2 h	$943 \pm 96$	1–10	330–210	$170 \pm 25$	Alamedin River;	silt	30	2.65
98-Koch-Q2	TIEN98-1	$5.01 \pm 0.32$	IRSL	150°C/2 d	780/2 h	$(679 \pm 76)$	1–10	330–210		Chu basin Djuanarik River;	silt	4	0.20
			IRSL	170°C/2 d	780/2 h	$(589 \pm 81)$	1–50	330–210		Kochkor basin			
			TL	160°C/2 d	400/3 d	$(644 \pm 79)$							
			TL	160°C/2 d	FSL/8 h	$742 \pm 91$							
SCT/091699	TIEN99-2	$4.45 \pm 0.34$	IRSL	160°C/2 d	780/2 h	$639 \pm 45^i$	1–40		$128 \pm 13$	Djergetal River;	sandy silt	2.7	0.30
						$667 \pm 87$			$150 \pm 23$	Naryn basin			
SCT/091899	TIEN99-3	$4.51 \pm 0.26$	IRSL	160°C/2 d	780/2 h	$423 \pm 35$	1–30	260–390	$93.8 \pm 9.0^j$	Djergetal River;	sandy silt	1.7	0.30
			TL	145°C/2 d	FSL/6.5 h	$644 \pm 57$			$143 \pm 15$	Naryn basin			

<sup>a</sup> Sample preparation and measurements at the Desert Research Institute, Reno.

<sup>b</sup> Polymineralic, noncarbonate, detrital 4–11- $\mu$ m-diameter size fraction was used for all TL and IRSL measurements. Luminescence was detected at the  $420 \pm 20$  nm spectral region (band pass 390–470 nm at 1% cut). Laboratory sample preparation procedures follow Berger [1990].

<sup>c</sup> Effective dose rate,  $D_R$ , is derived from independent measurements of U, Th, K, and water concentration.  $D_R$  is calculated with the conversion factors and equations given by Berger [1988] and includes a cosmic ray component varying from 0.03 to 0.17 with estimated average depth, from the data of Prescott and Hutton [1988].

<sup>d</sup> The chosen preheat duration and heating and duration (days) (to empty laboratory-filled electron traps). Pre-heating was applied after bleaching.

<sup>e</sup> Bleaching protocol (FSL is full solar spectrum at Reno; 400 means laboratory Hg vapor lamp with 400–750 nm passed; 780 means >780-nm solar spectrum passed), and duration (in h, hours, or d, days).

<sup>f</sup> Weighted mean equivalent dose plus average error over time/temperature interval. A weighted-saturating-exponential regression and error model [Berger et al., 1987] was employed for all samples. For some IRSL samples, interaliquot scatter was minimized by short-shine normalization (to natural signals) [Ollerhead et al., 1994].

<sup>g</sup> The readout (LED-on) time interval or the temperature interval (if TL) for which  $D_E$  is calculated.

<sup>h</sup> Luminescence age  $t = D_E/D_R$ .

<sup>i</sup> Weighted mean of the three equivalent dose values in parentheses.

<sup>j</sup> Measurement rejected because it is significantly different from the TL measurement of the same sample, and the TL age is not significantly different from the age of sample TIEN99-2, collected from a stratigraphically similar terrace  $\sim 1.5$  km away [Thompson, 2001].

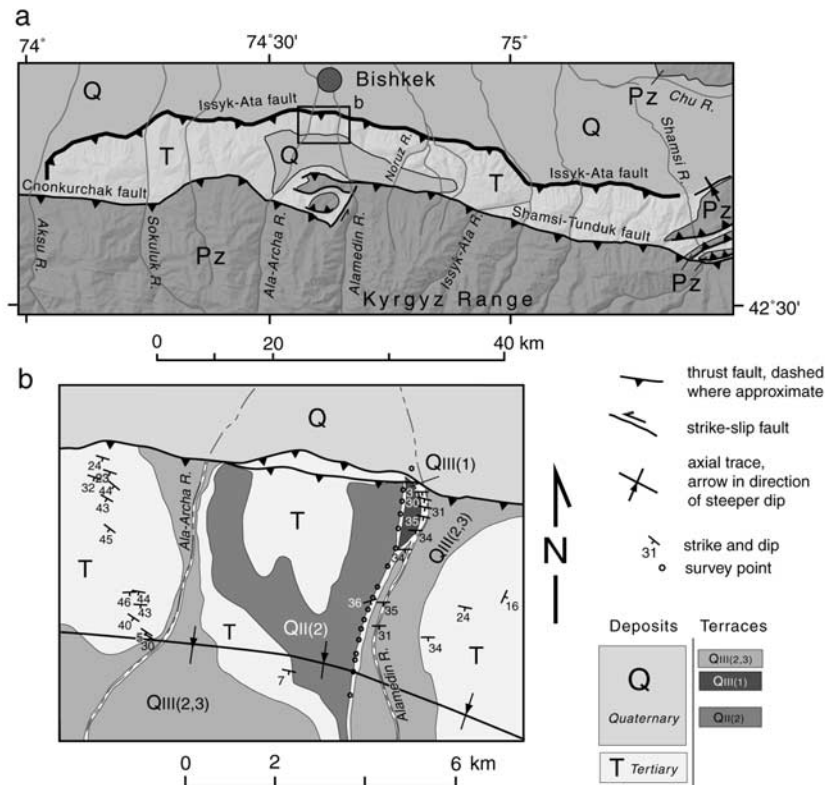


**Figure 4.** (a) Tectonic map of the southern Chu basin, showing major faults, geologic units, and rivers on a shaded-relief topographic base. Pz, Paleozoic; T, Tertiary; Q, Quaternary. (b) Geologic map of the Alamedin River site, showing the Issyk-Ata fault, terraces, strikes and dips of Tertiary strata, and differential GPS survey points.

suggests that straths on the hanging walls of reverse faults and on the crests of anticlines, with a few meters of alluvial cover, formed later than straths on the footwalls of faults and on the flanks of folds, with tens of meters of alluvial cover [Thompson, 2001]. Second, the stratigraphic contact between gravel and overlying fine-grained sediments approximates the transition from aggradation or planation of a floodplain by the river channel to incision by the river channel, after which only overbank sediments, and eventually only loess and colluvium, could accumulate on the newly formed terrace.

#### 4. Fault Slip Rates

[18] Profiles of deformed river terraces, trench walls, natural exposures of faults, and radiocarbon and luminescence ages provide data for measuring fault slip rates. If a displaced terrace is preserved in both the hanging wall and footwall of a fault, the slip rate calculation is straightforward (Appendix A). If deformed terraces in a hanging wall are offset against an aggrading surface in a fault footwall, we calculate fault slip rate using fault-related fold growth recorded in the hanging wall (Appendix B). Because most late Quaternary faults that we examined lie within the well bedded Cenozoic strata of intermontane basins, mapped bedding dips and fault traces allowed us to draw preliminary cross sections that use simplified fault-related fold geometries [Suppe, 1983; Suppe and Medwedeff, 1990] and

predict active and inactive axial surfaces and subsurface fault geometry in the absence of subsurface data. The terraces that cross these active faults have been deformed less than the Cenozoic strata. Consequently, the terraces are angular unconformities that can be used, like growth strata, to test the geometric and kinematic predictions of fault-related fold deformation (Appendix B).

[19] Slip rates are presented with the most probable value and minimum and maximum 95% confidence values resulting from Monte Carlo simulations of uncertainties described in Appendix C. Unless specified otherwise, all uncertainties in the text represent the  $2\sigma$  or 95% confidence interval. We calculated the slip rate of the most active fault (or faults) in each of five basins (Figure 2). All these fault zones show signs of Holocene activity and multiple slip events since  $\sim 140 \times 10^3$  years B.P.

##### 4.1. Issyk-Ata Fault, Chu Basin

[20] The Issyk-Ata fault defines the northern deformation front for the central Tien Shan between  $\sim 74^\circ\text{E}$  and  $\sim 75^\circ\text{E}$  longitude (Figures 2 and 4a). It extends at least 120 km from the Aksu River east to its surface termination near the Shamsi River [Abdrakhmatov, 1988]. As a moderately dipping thrust to reverse fault at the surface, the Issyk-Ata fault places Neogene sandstone and siltstone over Quaternary gravel. The Issyk-Ata fault merges at its western terminus with the Chonkurchak fault, which marks the boundary between pre-Cenozoic basement at the Kyrgyz Range front and late

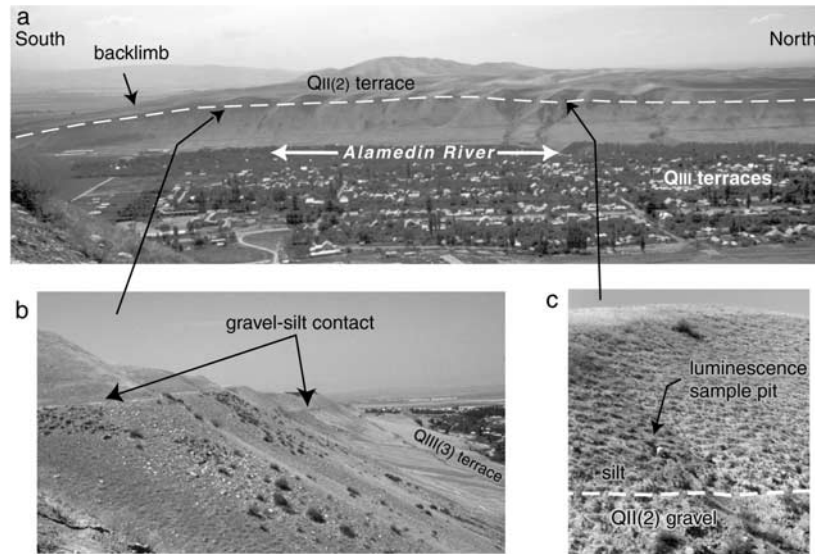


**Figure 5.** (a) Folded terraces of the Alamedin River (river flows to the north). Note the south dipping QII(2) terrace surface at the south end of the photo (labeled “backlimb”); the contact between fluvial gravel and overlying silt is indicated by the white dashed line. Inset QIII(2) and QIII(3) terraces are in the foreground, under houses and trees. (b) View to the north along the contact between gravel and silt for the QII(2) terrace. (c) Pit excavated for collection of silt for luminescence dating, located  $\sim 2.5$  m above the contact with fluvial gravel.

Cenozoic deposits in the western Chu basin (Figure 4a). Farther east, between the Ala-Archa and Alamedin Rivers, the Chonkurchak fault steps north, and its eastward continuation is called the Shamsi-Tunduk fault. Late Pleistocene terraces near the Alamedin River are folded along portions of the Shamsi-Tunduk fault, although the amplitude of folding indicates minor late Quaternary surface shortening compared with the folded and faulted terraces above the Issyk-Ata fault. We interpret the Issyk-Ata fault as a splay from the Shamsi-Tunduk/Chonkurchak fault beneath the southern margin of the Chu basin. We estimate a slip rate for the Issyk-Ata fault on its central portion, where it crosses the Alamedin River (Figure 4b).

[21] Nested river terraces can be traced along the Alamedin River for  $\sim 12$  km from within the Kyrgyz Range front to the Issyk-Ata fault, just south of Bishkek (Figure 4). Starting  $\sim 5$  km south of the Issyk-Ata fault, between the Alamedin and Ala-Archa Rivers, river terraces cover a prominent row of hills underlain by south dipping Neogene strata (Figures 4b and 5) [Abdrakhmatov, 1988; Chediya, 1986]. Terrace risers along the Alamedin River expose a nearly continuous section of Neogene sedimentary rock dipping  $\sim 30^\circ$  to  $36^\circ$  S beneath the uplifted terrace section (Figures 5a and 6). We did not find Neogene strata outcropping south of the elevated portion of the terrace. North of the Issyk-Ata fault, in the footwall, coalescing alluvial fans show that the Alamedin River is aggrading there.

[22] The contact between a thin layer of fluvial gravel, deposited on the Tertiary bedrock strath, and overlying fine-grained sediments for the QII(2) terrace shows a back-tilted section along the southern edge, particularly if rotated to remove the  $\sim 1.7^\circ$  modern river gradient (Figure 6). The back-tilted segment, which we interpret as a growing backlimb of a fault-bend fold, rises to  $103 \pm 1$  m above the

modern river level for 1.7 km. The top of the backlimb and the northern end, close to the fault, are higher. This variation in height could be due to steep faults or fault-related folding that we did not detect in our mapping of Neogene strata, or it could mean that an older terrace,  $\sim 125$  m above modern river level, was inset by a terrace  $\sim 103$  m above modern river level. The loess on top of the terrace gravel is up to 30 m thick and obscures the variation in height of the gravel contact in distant views of the terrace (Figure 5a).

[23] We analyze the QII(2) terrace deformation using simple fault-bend fold models of structural growth (Appendix B). To test the geometry and kinematics of a structural interpretation, we compare the terrace profile to predictions of the deformation of a flat unconformity (river terrace) due to slip on an inferred fault (see Figure B1).

[24] A lack of structural data south of the high section of the QII(2) terrace along the Alamedin River hinders analysis of fold growth. A more complete analysis of fold growth is possible for the Akchop Hills fault in the Kochkor basin, described below. Nevertheless, the amount of fault slip may be calculated from the difference in heights of the QII(2) terrace across the fold backlimb ( $h_1 - h_2$ ), from  $\psi$ , the angle between the slope of the terrace backlimb and the stream gradient, and from  $\delta_1$ , the angle between the fault and the stream gradient, which is assumed equivalent to the angle between the bedding and the stream,  $\alpha_1$  (Appendix B, Figure B1).

[25] We interpret the  $\sim 36 \pm 2^\circ$  difference between the dips of Tertiary strata under the elevated terrace and the present gradient of the river to reflect  $\delta_1$ . To estimate  $\delta_2$  (the angle of the fault south of the backlimb) we searched equation (B2) iteratively for values consistent with measurements of  $\delta_1$  and  $\psi$ . A line fit to three surveyed points that define the QII(2) terrace backlimb makes an angle of  $\psi =$



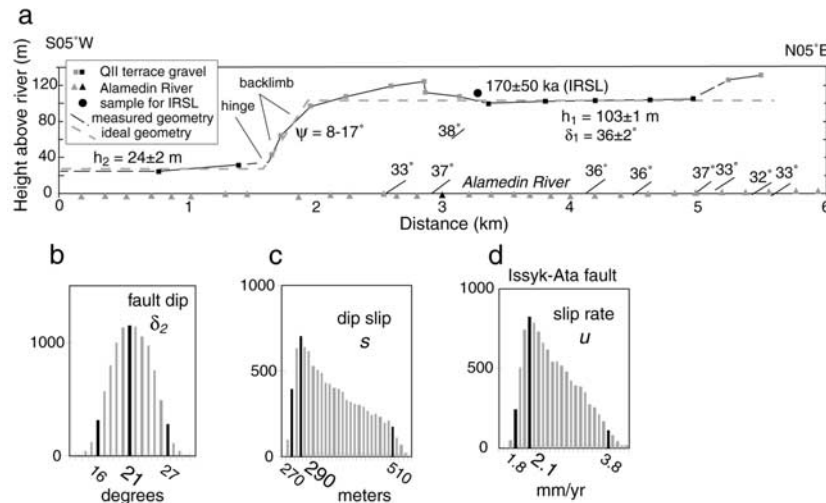


**Figure 6.** (a) Alamedin River profile, showing the deformed QII(2) terrace west of the river, the location and age of the sample collected for luminescence dating, and the apparent dips of Neogene strata exposed below the terraces. Points along the QII(2) terrace are from differential GPS surveying. Points along the Alamedin River are from 1:25,000-scale topographic maps with a 5-m contour interval (shaded) and differential GPS (solid). We removed the modern river gradient by rotating the data about a horizontal axis so that the  $x$  axis is parallel to the gradient of the river. Apparent dips of strata have been similarly rotated. Solid lines connect surveyed points with continuous exposure; solid dashed line indicates our interpretation of a hinge and secondary folding near the top of the hinge and at the northern front. The dashed shaded line schematically illustrates the simplification of the geometry of the terrace; this line is constrained by the black points that define the terrace south and north of the fault bend. We base the slip rate calculation on this simplified geometry with the values of  $h_1$ ,  $h_2$ ,  $\psi$ , and  $\delta_1$  indicated. The method for calculating slip rate is described in Appendix B. (b) Histogram showing the predicted value of  $\delta_2$ , based on equation (B2) in Appendix B. The solid bars indicate the 95% confidence minimum and maximum, and the most probable value. (c) Histogram showing the predicted amount of dip slip on the Issyk-Ata fault since formation of the QII(2) terrace. (d) Histogram showing the probability distribution of slip rate.

$9.5 \pm 1.5^\circ$ S with the surface, but one pair of these points yields  $17^\circ$  (Figure 6). Because most violations of the ideal fault-bend fold geometry will reduce measured values of  $\psi$  [Thompson *et al.*, 1999], we use a range of backlimb angles of  $\psi = 8-17^\circ$ S in the error analysis. The change in height of the terrace across the backlimb of the fold,  $h_1 - h_2$ , is given by the difference between the height of the flat middle section of the uplifted terrace,  $h_1$  ( $103 \pm 1$  m), and the height of a point surveyed south of the growing backlimb (with an assigned uncertainty twice the value of the measured one),  $h_2$  ( $24 \pm 2$  m).

[26] An IRSL age of  $170 \pm 50$  ka gives a limiting minimum age of the QII(2) terrace along the Alamedin River (Figure 3 and Table 2). The IRSL age was measured on silt sampled from  $\sim 2.5$  m above an exposed contact between river gravel and  $\sim 30$  m of overlying fine-grained material (Figures 5 and 6). We interpret the fine-grained layer as mostly loess, although overbank sediment may be preserved or mixed with loess near the base of the sediment. To improve precision, we use the pooled age of  $141 \pm 17$  ka for the QII(2) terrace in our calculation (Appendix C).

[27] Solving equation (B2) for  $\delta_2$  yields a value for fault dip south of the fold of  $18 \pm 6^\circ$ S, and equation (B1) yields  $290 +230/-20$  m of fault slip. The slip rate on the Issyk-Ata fault at the Alamedin River is  $2.1 +1.7/-0.3$  mm/yr (Figure 6).

[28] Equation (B3) predicts that the modern Alamedin River has risen  $53 +128/-17$  m since QII(2) formation, which corresponds to a footwall aggradation rate of  $0.5 +1.0/-0.1$  mm/yr. This rate is consistent with the  $0.6 \pm 0.3$  mm/yr aggradation rate of Plio-Pleistocene gravel measured near the Noruz River,  $\sim 15$  km east of the Alamedin River (Figure 4) [Bullen *et al.*, 2001].

#### 4.2. Akchop Hills and South Kochkor Faults, Kochkor Basin

[29] Active faults and folds deform the southern margin of the Kochkor basin, an east-west trending intermontane basin south of the Kyrgyz Range (Figures 2 and 7a). The South Kochkor fault follows the southern margin of the basin, placing Paleozoic metamorphic and igneous rock of the Terskey Ala-Too over weakly cemented Neogene sedimentary rocks [Fedorovich, 1935; Sadybakasov, 1972; Schulz, 1948; Tarasov, 1970]. Although this fault and proximal splays cut late Quaternary river terraces and alluvial fans, most of the late Quaternary surface deformation occurs several kilometers to the north, within the basin, where it is expressed by a band of hills of folded Miocene to Pliocene Djuanarik Formation sandstone and siltstone (Figure 7b). Erosion and deposition by the Djuanarik River, which flows northward across the southern margin of Kochkor basin, have produced multiple, nested river terra-

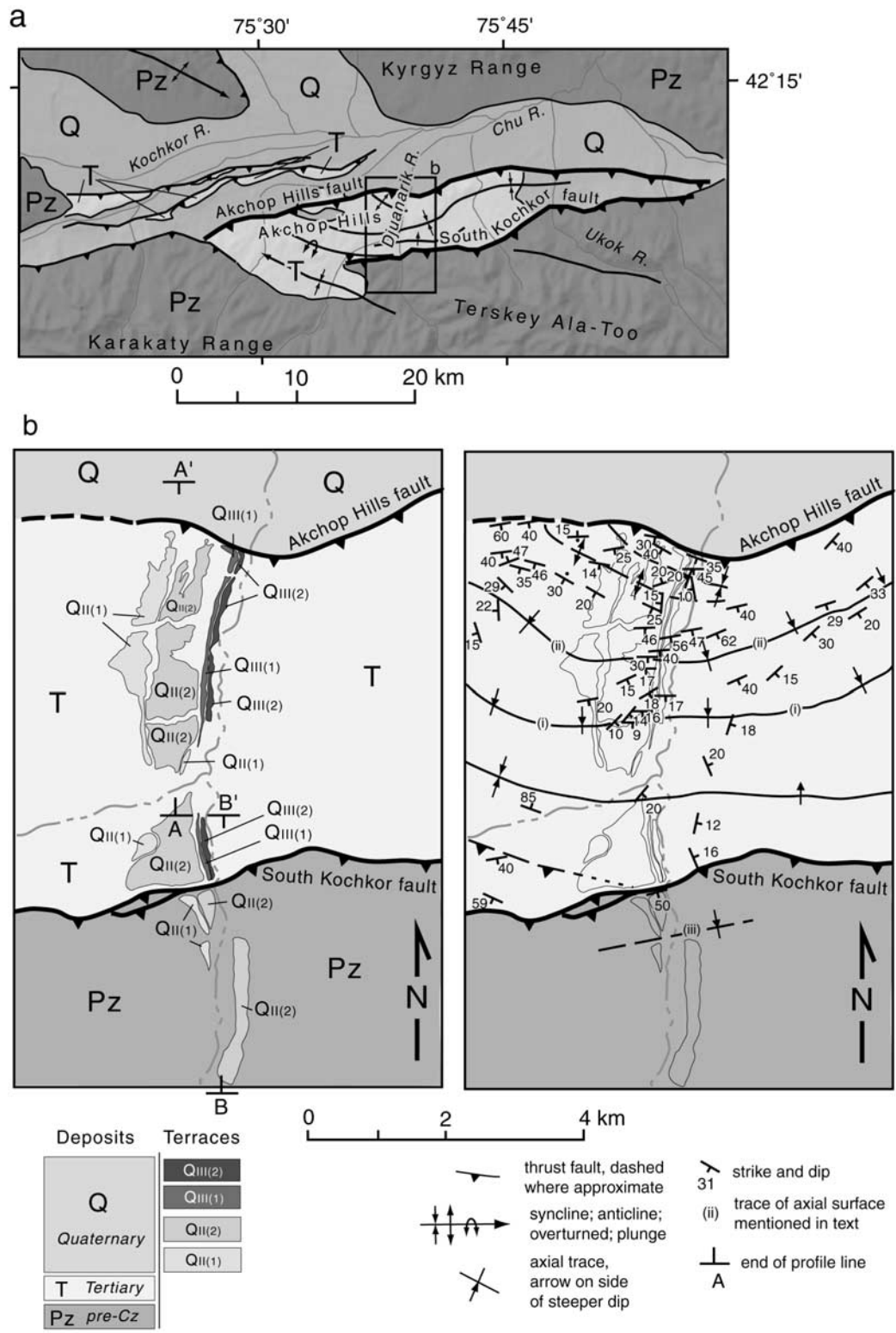


**Figure 7.** Maps showing active deformation in the southern Kochkor basin. (a) Simplified geologic map. Pz, Paleozoic; T, Tertiary; Q, Quaternary. The Akchop Hills consist of folded Tertiary strata in the hanging wall of the Akchop Hills fault. (b) Geologic maps of the Djuanarik River area. Map on left shows nested terraces along the west bank of the Djuanarik River; map on right shows strikes and dips of underlying strata, axial traces, and outlines of terraces. Axial traces labeled i, ii, and iii are discussed in the text and in later figures. Surveyed points along the extensive QII(2) terrace constrain our analyses of slip rate for the Akchop Hills fault (profile line A-A'; map on left) and South Kochkor fault (profile line B-B'; map on left).

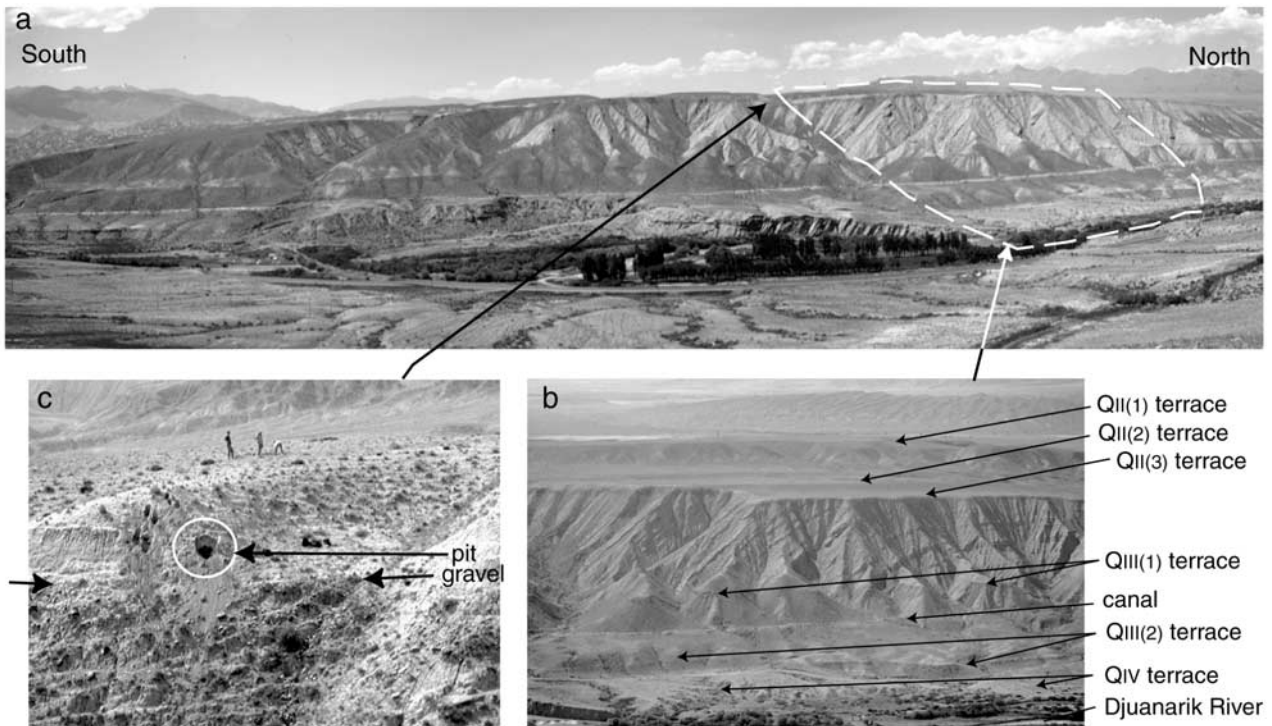


**Figure 8.** Nested terraces along the west side of the Djuanarik River, Kochkor basin. (a) View to the west of terraces and Djuanarik River (the river flows north). White dashes outline area in Figure 8b, and solid arrow indicates location of Figure 8c. (b) View to the northwest of strath terraces. Surfaces are labeled. Notice exposed Djuanarik Formation sandstone layers that are folded (photo by M. Miller). (c) View to the south of pit excavated for the collection of silt for luminescence dating on the QII(2) terrace (marked with a white circle). Short arrows mark the contact between fluvial gravel and overlying fine-grained sediments.

ces that are progressively deformed across the growing Akchop Hills [Fedorovich, 1935] (Figure 8). We surveyed profiles along five river terraces and mapped the underlying strata on the west side of the Djuanarik River to evaluate the subsurface geometry and rates of slip on faults along the southern margin of Kochkor basin (Figures 7b and 9). The presence of an abrupt topographic front at the northern edge of the Akchop Hills and the south dipping strata underlying the hills indicate that the Akchop Hills overlie a south dipping thrust fault (the Akchop Hills fault) that connects south of the range front with the South Kochkor fault. We calculate slip rates for both faults from measurements of a deformed late Quaternary terrace, starting with the faster slipping Akchop Hills fault.

#### 4.2.1. Akchop Hills Fault

[30] Profiles of three river terraces along the west side of the Djuanarik River, rotated to remove the  $\sim 0.7^\circ$  modern river gradient, show progressive vertical movement and development of back-tilted sections (Figure 9). Because the structure is well approximated by kink-style geometry with relatively angular bends (axial surfaces) (Figures 7b and 9), we can use fault-bend fold theory to infer the geometry and kinematics of fault slip at depth (Appendix B). Synclinal axial surfaces, in particular, are angular along the Djuanarik River, and two synclinal axial surfaces in the Neogene stratigraphy in the backlimb of the fold (Figure 7b) also mark bends in river terraces QII(2) and QIII(1) (Figure 9a),

indicating that the axial surfaces are presently active. We assume that faults are parallel to hanging wall strata in the backlimb of the fold (i.e., no hanging wall cut-off).

[31] We interpret the southern synclinal bend to result from fault-bend folding above a thrust ramp that steepens from  $\delta_2 = 9 \pm 2^\circ$  S to  $\delta_1 = 18 \pm 2^\circ$  S (Figure 9c and Appendix B). We calculate the slip on the underlying fault using the difference in height of the QII(2) terrace across axial surface *i* (Figure 9). The predicted backlimb angle (equation (B2)) matches the measured backlimb angle well, supporting the geometric interpretation (Figure 9c).

[32] TL and IRSL analyses of massive silt from the base of a  $\sim 4$ -m-thick deposit overlying the fluvial gravel of the QII(2) terrace yield an age of  $128 \pm 26$  ka since last exposure to light (Table 2 and Figures 3, 8, and 9). We use the pooled age of the four QII(2) terraces,  $141 \pm 17$  ka, as the age of terrace formation in our slip rate calculation (Appendix C). The dip-slip rate, using parameters described above and inserted into equation (B1), is  $2.9 + 1.6 / -0.7$  mm/yr (Figure 9d).

#### 4.2.2. South Kochkor Fault

[33] We calculate a slip rate for the South Kochkor fault using the offset QII(2) terrace at the range front (Figures 7b and 10a). A profile of the QII(2) terrace across the fault extends 2.5 km south of the range front and a similar distance north and shows an abrupt bend (axial surface *iii* in Figure 7b) and a back-tilted section beginning  $\sim 600$  m

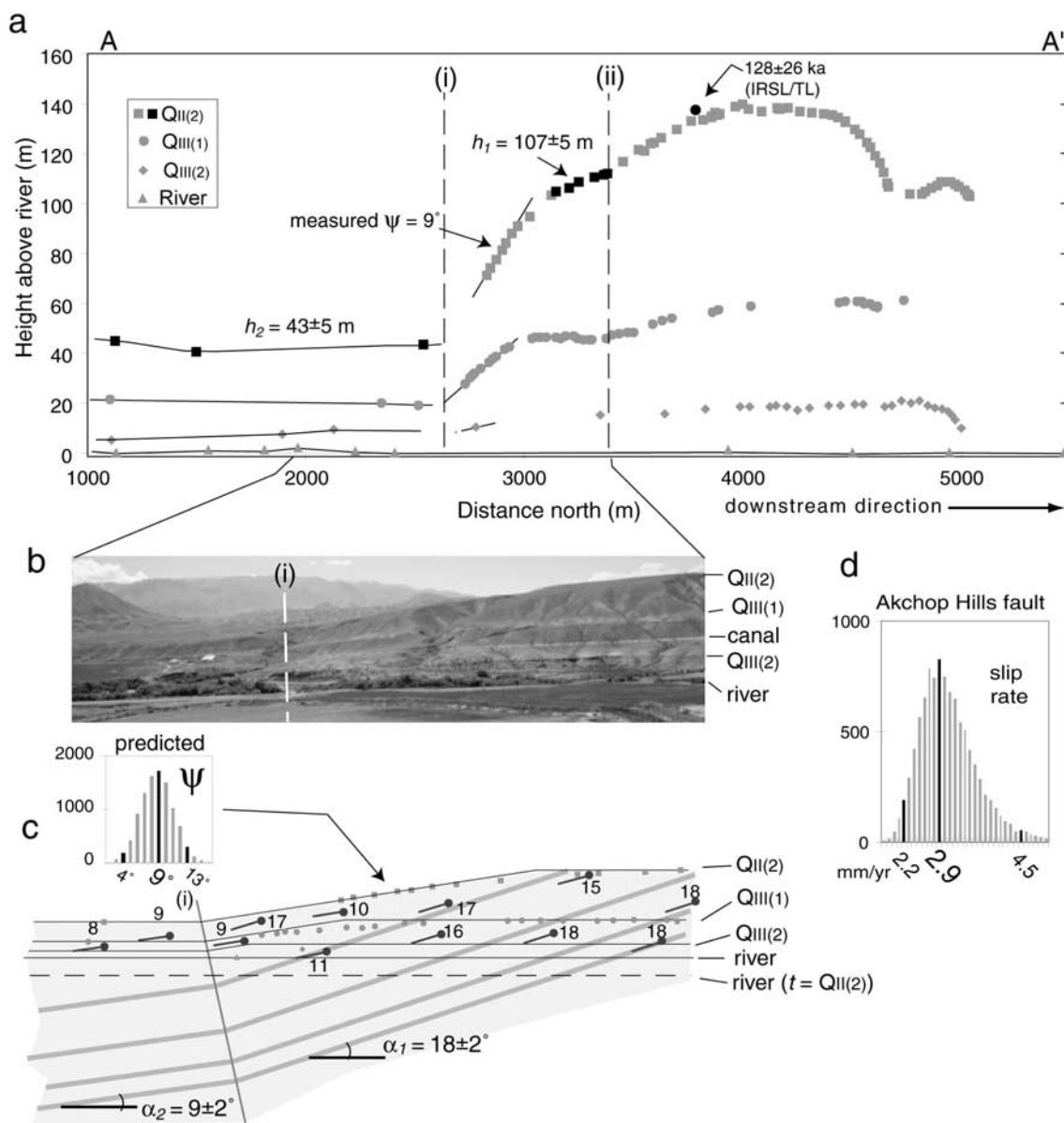


**Figure 9.** (a) Vertically exaggerated river terrace profiles along the Djuanarik River. Profiles were rotated counterclockwise  $0.7^\circ$  so the horizontal axis would parallel the modern river. Note the progressive limb rotation and kink band migration recorded by the backlimbs of the QIII(1) and QII(2) terraces north of active axial surfaces i and ii; we infer a backlimb for the QIII(2) terrace but did not sample enough points to measure it. The solid squares on the QII(2) terrace were used to define the heights of the terrace across axial surface i. (b) Photo of the backlimb of the Akchop Hills anticline across axial surface i, showing the QII(2), QIII(1), and QIII(2) terraces. (c) Cross section across axial surface i, showing apparent dips of Pliocene Djuanarik Formation strata and surveyed points along the terraces and modern river. Thick shaded lines schematically illustrate dipping strata across the fold. Thin solid lines show the predicted terrace profiles that assume the terraces are deformed by ideal fault-related folding (see Appendix B). Inset shows the predicted backlimb angle (equation (B2) in Appendix B). Horizontal dashed line shows inferred position of the river at the time of QII(2) terrace formation. (d) Histogram showing slip rate probability distribution for the Akchop Hills fault based on equation (B1) in Appendix B.

south of the fault (Figure 10a). Within  $\sim 100$  m of the fault the gravel contact of the QII(2) terrace folds into an anticline next to the fault scarp. In the footwall the QII(2) terrace and the inset QIII(1) terrace tilt to the south for a distance of  $\sim 1$  km. We interpret the back-tilting of the

terrace in the hanging wall as the result of rotation by a curved fault. The footwall tilt is due to either footwall fault-related folding of the South Kochkor fault or a gradual change in dip of the Akchop Hills fault underlying the terraces.

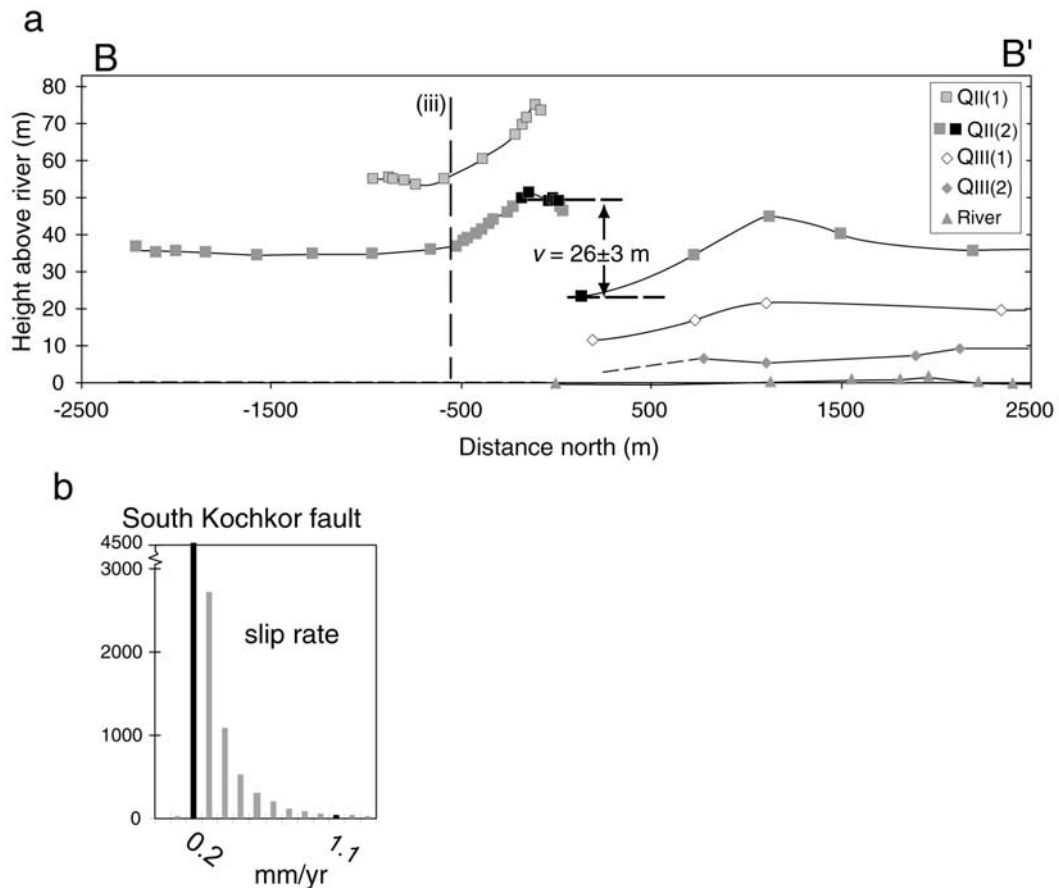


**Figure 10.** (a) Profile of river terraces across the South Kochkor fault, showing terrace correlation and folding of the terraces in the hanging wall across axial surface (iii). Black points and horizontal dashed lines indicate the vertical separation used in the slip rate calculation. (b) Histogram showing slip rate calculation for the South Kochkor fault. The 0.2 mm/yr bin contains the minimum slip rate (2.5% tail). Adding another significant digit to the histogram bins yields a 0.17 mm/yr minimum slip rate.

[34] We calculate a slip rate using the  $26 \pm 3$  m difference in height between six surveyed points in the hanging wall and one surveyed point in the footwall that is closest to the fault scarp. The active trace of the South Kochkor fault is not exposed at the range front. An older trace exposed in the hanging wall dips  $\sim 45^\circ$ S, and juxtaposes granite against Neogene sandstone [Sadybakasov, 1972]. On the basis of the map pattern of the fault, which suggests a moderate to steep dip, the dip is represented by a trapezoidal probability distribution with a maximum likelihood of  $30\text{--}70^\circ$ S (Appendix C). The slip rate of the South Kochkor fault is  $0.2 +0.9/-0.03$  mm/yr (Figure 10b).

#### 4.3. Kadjerty and Central Naryn Faults, Naryn Basin

[35] The Naryn Valley occupies one of the largest intermontane basins in the Kyrgyz Tien Shan and contains abundant evidence for Quaternary shortening [Burbank et al., 1999; Makarov, 1977; Sadybakasov, 1990; Schulz, 1948]. Much of the late Quaternary deformation is associated with two south vergent thrust faults that reach the surface in the northeastern and north central portions of the basin (Figures 2 and 11). Both the Central Naryn and Kadjerty faults are continuous for  $\sim 100$  km, with the mapped trace of the Central Naryn fault extend-

ing farther east and the Kadjerty fault extending farther west.

[36] The Akchatash fault and associated folds separate the northern margin of Naryn basin from the Moldo-Too Range [Makarov, 1977] (Figure 11). Late Quaternary terraces that cross the boundary between basin and range do not seem to be deformed. In several locations this fault cuts a Plio-Pleistocene conglomerate unit, but in others, anticlinal folding of the preorogenic erosion surface and an unconformable contact between pre-Cenozoic “basement” and Cenozoic strata mark the basin boundary. The anticlinal folding at the basin margin seems to indicate the transfer of fault slip from a north dipping crustal ramp underlying the Moldo-Too to the gently north dipping Kadjerty and Central Naryn faults that penetrate the northern Naryn basin. We have calculated the slip rates for the Kadjerty and Central Naryn faults along the south flowing Kadjerty River, a tributary to the west flowing Naryn River.

##### 4.3.1. Kadjerty Fault

[37] The Kadjerty fault crosses several nested terraces in the Kadjerty River valley,  $\sim 7$  km south of the range front (Figures 11b and 12). On the east side of the Kadjerty River the fault cuts as many as five terrace levels by progressively

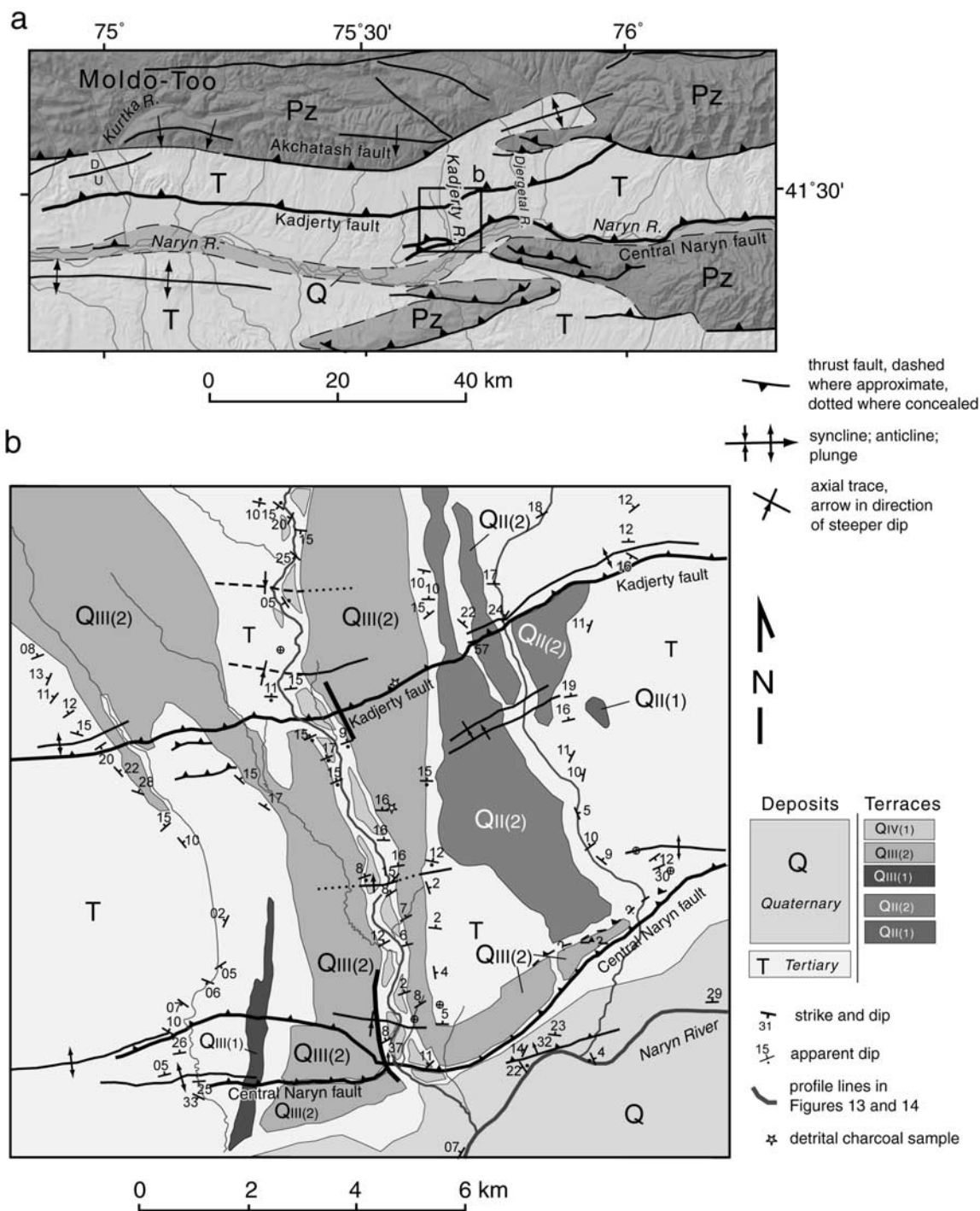


**Figure 11.** (a) Simplified geologic map of northeastern Naryn basin. Pz, Paleozoic; T, Tertiary; Q, Quaternary. The Kadjerly and Central Naryn faults appear to accommodate most of the shortening at the surface across the northern Naryn basin margin. We have evaluated the slip rates of the Kadjerly and Central Naryn faults along the Kadjerly River (box shows area of Figure 11b). (b) Geologic map along the Kadjerly River, showing dips of Tertiary strata, fault and fold traces, and river terraces.

greater amounts from a late Holocene terrace adjacent to the modern floodplain to the QII(2) terrace that marks the divide with the adjacent drainage (Figure 12a). Anticlinal folding and the preservation of hanging wall cutoffs indicate that total fault displacement is less than a few kilometers (Figure 11b).

[38] Profiles across the fault scarp that crosses the broad QIII(2) terrace east of the Kadjerly River show vertical separations from ~8 m at the east end increasing to ~12 m near the west edge of the tread. We calculate the slip rate of the Kadjerly fault using a profile at the west end of the terrace tread that lies close to the adjacent terrace riser to the inset

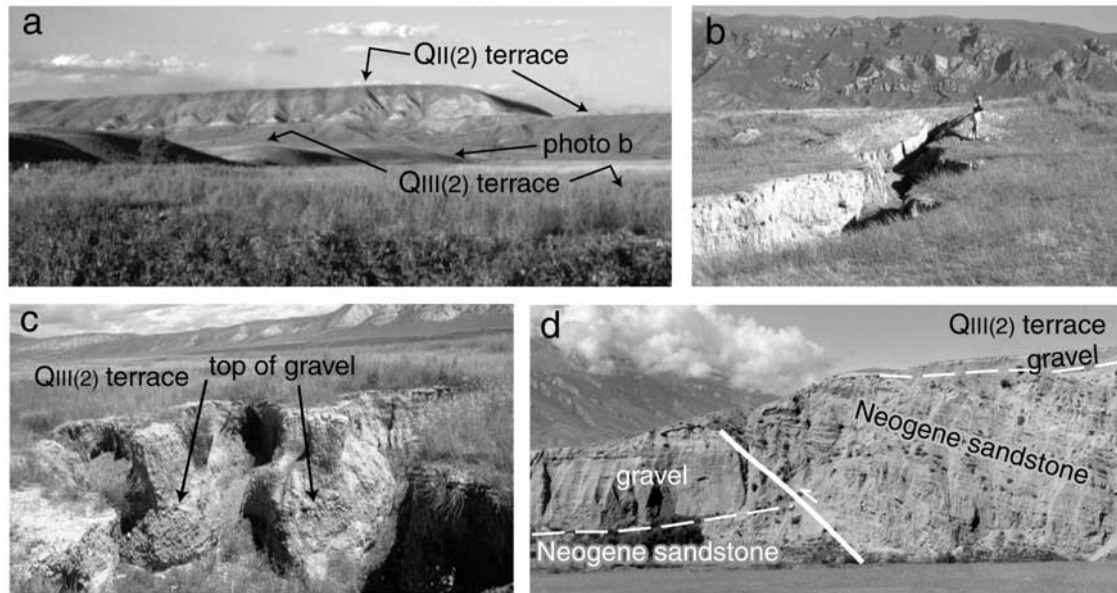


**Figure 12.** (a) Kadjerty fault scarp cutting nested terraces. View is to the northeast along the scarp. The fault scarp across the QII(2) terrace (in the distance) has a vertical separation of  $\sim 80$  m; the fault scarp across the QIII(2) terrace to the left has a vertical separation of about 10 m. (b) Gully and trench across the QIII(2) fault scarp near the QII(2) terrace riser exposes terrace gravel and charcoal. Detrital charcoal from the top of the fluvial gravel dates to  $14.1\text{--}15.4 \times 10^3$  cal years B.P. (c) A gully in the QIII(2) terrace between the Kadjerty and Central Naryn faults exposes fluvial gravel and overlying fine-grained sediments. Two detrital charcoal fragments collected above the gravel contact in this exposure date to  $13.5\text{--}14.1 \times 10^3$  cal years B.P. View is to the north. (d) Central Naryn fault exposure along the Kadjerty River. View is to the southwest. The exposed fault dips  $37 \pm 2^\circ\text{N}$ . Neogene strata in the hanging wall dip  $\sim 11\text{--}15^\circ\text{N}$ . The Kadjerty River flows south along the base of the exposure. Notice thicker accumulation of late Quaternary gravel in the footwall of the fault.

QIV terraces (Figures 11 and 13). Here, the vertical separation of the QIII(2) terrace is  $12.4 + 0.9 / - 0.8$  m. Although the fault plane is not exposed in either valley wall of the Kadjerty River, we calculate the fault dip by measuring the scarp locations on the QIII(2) terrace and on the adjacent QIV terrace. Using the average trend of the QIII(2) terrace scarp ( $\text{N}66^\circ\text{E}$ ) and the QIV terrace scarp ( $\text{N}71^\circ\text{E}$ ) to establish the

strike of the fault, we calculate a fault dip of  $29 \pm 5^\circ\text{N}$  at the QIII(2)/QIV riser. The uncertainty in the dip incorporates the  $5^\circ$  difference in strike above and below the riser and the uncertainties in the locations of the fault within the scarps on the upper and lower terrace surfaces. A decrease in terrace height north of the profile in Figure 13 suggests that the fault dip decreases to  $\sim 10^\circ\text{N}$  at depth.

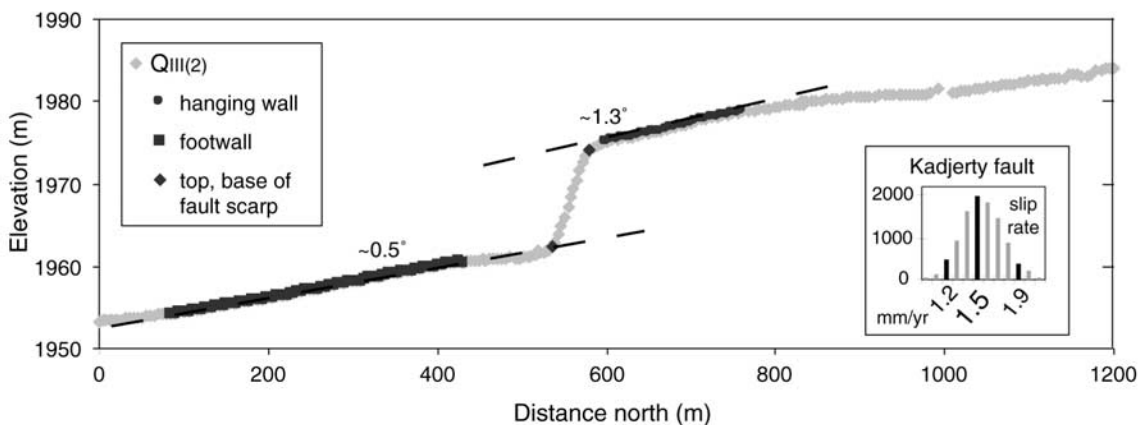


**Figure 13.** Profile of the QIII(2) terrace across the Kadjerty fault east of the Kadjerty River; location on Figure 11b. Solid circles, squares, and diamonds indicate the points used to define the surfaces on the hanging wall, footwall, and scarp face, respectively.

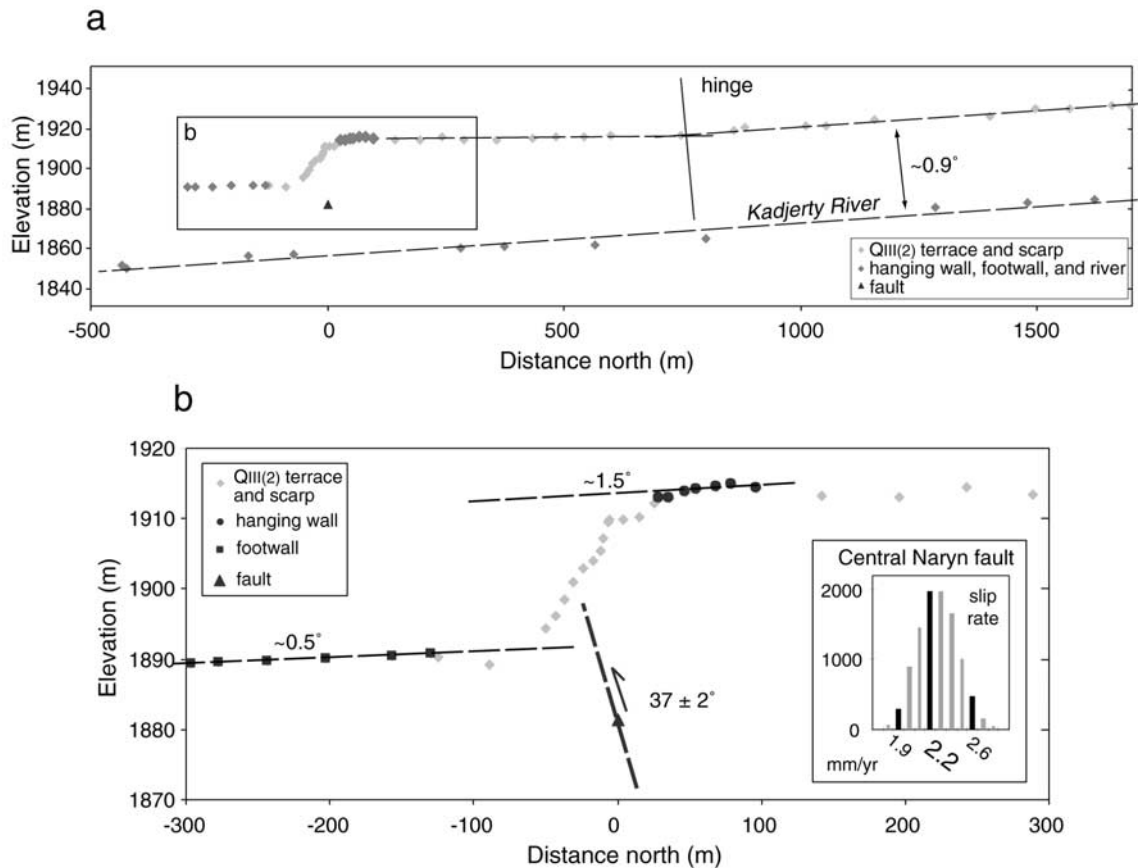


**Figure 14.** (a) Profile of the upper gravel contact of the QIII(2) terrace across the Central Naryn fault near the Kadjerty River; location shown on Figure 11b. The gradient of the QIII(2) terrace and the modern river are similar north of the labeled “hinge,” but south of the hinge, the terrace surface is subhorizontal, indicating that it has been rotated due to slip on the Central Naryn fault. (b) Close-up view of the profile across the fault scarp, showing the surveyed points used to define the hanging wall and footwall and the dips of those surfaces. A single point surveyed on the exposed fault surface and the measured dip are used to constrain the fault location in the slip rate calculation.

[39] Three radiocarbon analyses on detrital charcoal constrain the timing of river incision, floodplain abandonment, and formation of the QIII(2) terrace along the Kadjerty River (Figures 3, 11, and 12 and Table 1). The weighted age distribution of the three samples results in a  $13.7\text{--}15.3 \times 10^3$  cal years B.P. age range for the QIII(2) terrace gravel contact (Appendix C). Using the parameters outlined above, equations (A3)–(A6) yield a slip rate of  $1.5 + 0.4 / -0.3$  mm/yr (Figure 13).

**4.3.2. Central Naryn Fault**

[40] Two splays of the Central Naryn fault that cut QIII terraces west of the Kadjerty River merge into a single fault trace near the west river bank (Figure 11), where a ~40-m-high exposure shows that the Central Naryn fault dips  $37 \pm 2^\circ$  N (Figure 12d). A profile of the top of fluvial gravel on the QIII(2) terrace shows a small anticline near the fault scarp and a bend ~750 m north of the scarp. North of the bend, the terrace slopes  $0.9^\circ$  S, similar to the  $0.9^\circ$  S slope of the modern river (Figure 14a). South of the bend the terrace surface is subhorizontal, implying a back rotation that we attribute to changes in underlying fault dip. The change in terrace height, with the assumption of constant fault dip and

the recognized  $\sim 37^\circ$  N dip at the surface, is consistent with a fault dip of  $\sim 12^\circ$  N at depth.

[41] To evaluate slip rate, we determine the vertical separation of the terrace close to the scarp, confining our calculation to surveyed points in the hanging wall that are within 100 m of the fault exposure (Figure 14b). The vertical separation of the QIII(2) terrace is  $20.6 \pm 1.0$  m. A point surveyed on the fault plane constrains the location of the fault (point P in Appendix A). Using the known fault location, the  $37 \pm 2^\circ$  fault dip, and the age distribution described in Appendix C, the rate of dip slip for the Central Naryn fault is  $2.3 + 0.3 / -0.4$  mm/yr (Figure 14b).

**4.4. Oinak-Djar Fault, At-Bashi Basin**

[42] The south vergent Oinak-Djar fault (“Quaternary fault” of Makarov [1977]) appears to accommodate most of the late Quaternary shortening across the western and central At-Bashi basin (Figures 2 and 15). For most of its 80-km strike length the fault separates hills composed of steeply dipping Tertiary sediments and large late Quaternary fans (Figure 16). Although for much of its length a well-defined scarp indicates that the Oinak-Djar fault reaches the



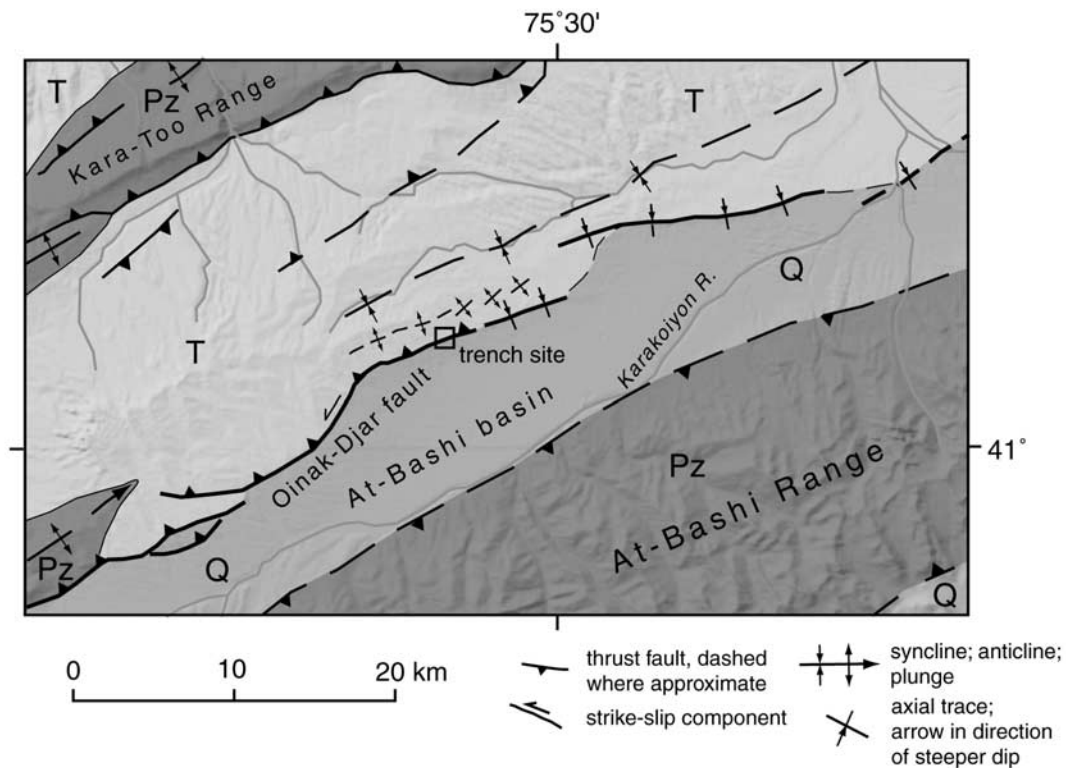


**Figure 15.** Simplified geologic map of the western At-Bashi basin. Pz, Paleozoic; T, Tertiary; Q, Quaternary. The Oinak-Djar fault marks the boundary between Tertiary strata and late Quaternary deposits and defines the southeast margin of deformation for the larger structure that separates the Naryn and At-Bashi basins. The Oinak-Djar fault reaches the surface along the western half of the mapped trace; to the east the fault is blind, and the surface expression is a fault-propagation fold with a sharp synclinal axial surface. A trench excavated across the fault (boxed area) provides data to measure slip rate.

ground surface, the thrust fault is concealed along its eastern portion as slip is transferred into growth of a fault-propagation fold. Right-stepping en echelon fold axes in the hanging wall of the fault and deflected drainages indicate a minor component of left-lateral shear to this fault [Makarov, 1977] (Figure 15).

[43] We excavated a 20-m-long trench across the Oinak-Djar fault where the fault has offset the head of an alluvial fan repeatedly during the late Quaternary Period (Figures 16 and 17a). Trench wall exposures reveal four thrust splays that displace a series of mudflow and fluvial deposits (Figure 17a). We correlate two deposits across the fault zone that contain detrital charcoal. The oldest correlative deposit (layer C in Figure 17a) is the lower of two layers of silty sand mudflow deposits that are interstratified with coarse sand and fine gravel alluvium. The younger correlative deposit (layer A in Figure 17a) contains coarse sand and fine gravel alluvium with a laminar silt layer at its base and is overlain by a silty sand mudflow deposit.

[44] We determine the slip rate of the Oinak-Djar fault by measuring vertical separations of layers A and C across the fault zone. In order to restore the anticlinal folding of layers A and C in the hanging wall we assume that the projected contacts dip  $8.4^{\circ}$ S, similar to the terrace surface immediately north of the trench (Figure 17b). Vertical separations of layers C and A are  $4.2 \pm 0.5/-0.3$  m and  $4.0 \pm 0.4/-0.3$  m, respectively. Radiocarbon ages of detrital charcoal frag-

ments indicate that layer C was deposited  $\sim 9.6-10.4 \times 10^3$  cal years B.P., and the laminar silt at the base of layer A was deposited  $\sim 9.0-9.3 \times 10^3$  cal years B.P. (Figure 17a and Table 1). This yields a slip rate of  $0.9 \pm 0.4$  mm/yr for layer C and a  $0.9 \pm 0.5/-0.4$  mm/yr slip rate for layer A. The pooled slip rate is  $0.9 \pm 0.3$  mm/yr for the Oinak-Djar fault (Figure 17b).

#### 4.5. North and South Kyrkungey Faults, Aksay Basin

[45] Only two faults appear to have significant late Quaternary slip rates in the eastern Aksay basin. These faults, which we call the North and South Kyrkungey faults, are part of a  $\sim 40$ -km-long system of folded hills that trend  $\sim 10$  km southeast of and parallel to the southeastern At-Bashi Range front [Makarov, 1977] (Figures 2 and 18). Our reconnaissance suggests that this fault system within the Aksay basin is more active than the North Aksay fault that defines the northern margin of the basin. Large moraines, formed during the last glacial period, are offset  $< 1$  m by the North Aksay fault; inset, younger moraines do not appear displaced. The North and South Kyrkungey faults cut alluvial terraces downstream of the moraines and show signs of recent offset in several locations. Both the North and South Kyrkungey faults appear to dip south, in a direction opposite of the North Aksay fault that marks the southern boundary of the At-Bashi Range. One possibility is that these faults form a basement-involved structural wedge

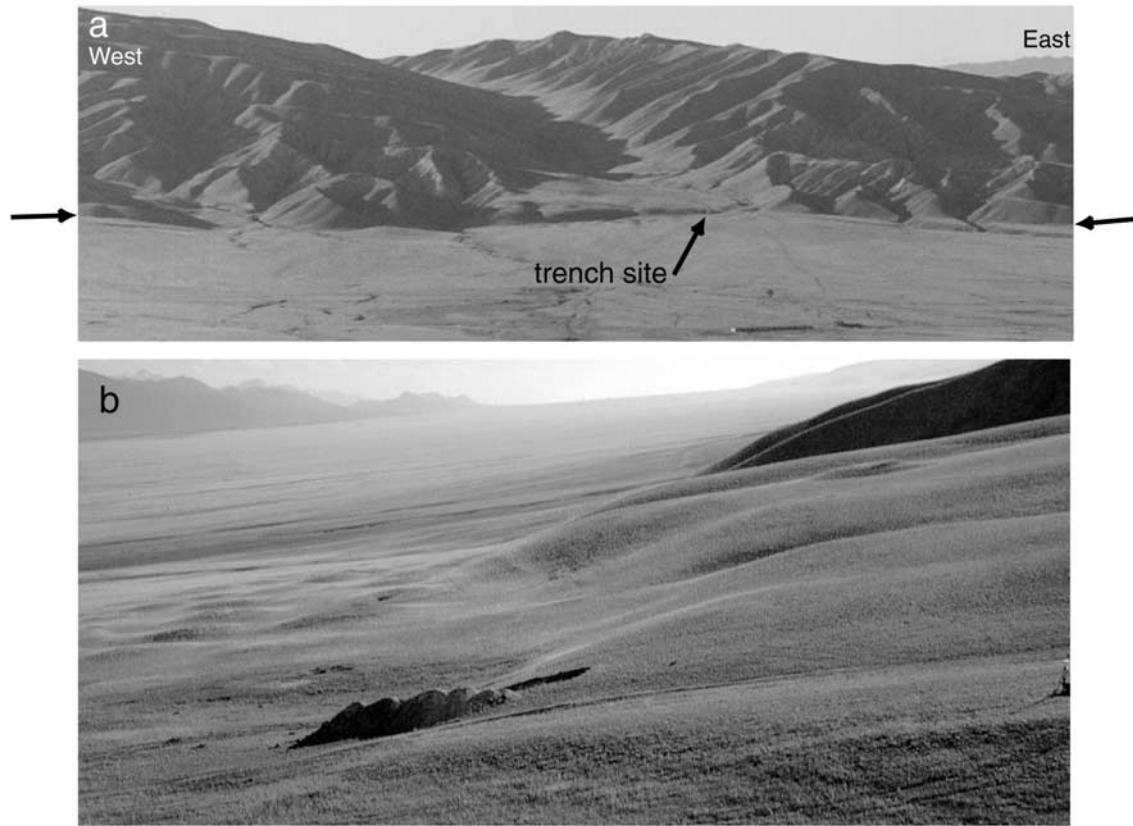


**Figure 16.** (a) View to the north of the Oinak-Djar fault scarp. The fault (between horizontal arrows) separates the hills of steeply dipping Tertiary strata in the hanging wall from the aggrading alluvial fans in the footwall. The trench site is situated in the eastern part of a wide wash in which multiple terrace levels are progressively displaced by recent slip on the fault. (b) View to the west along the Oinak-Djar fault scarp. The trench and spoil pile are in the foreground. The spoil pile is  $\sim 2$  m high. The mounds on the fan surface in the middle left of the photo are cultural sites of uncertain age and purpose.

that connects to the south vergent North Aksay fault at depth. Our mapping and slip rate evaluation of the two faults are crude, partly due to limited time in the field at this location and the poor exposure of underlying late Cenozoic strata. Despite the imprecision, the slip rates of these faults are low compared to those discussed above.

#### 4.5.1. North Kyrkungey Fault

[46] The North Kyrkungey fault displaces the heads of small Holocene fans and terraces southeast side up between the Djobogoshu River and the Kashkasu River (Figures 18 and 19). Elsewhere along the trace of the fault evidence of recent surface faulting is absent or unclear, suggesting that the fault does not reach the surface in all locations or consists of several short segments. However, an aligned row of folds to the northeast indicates that late Quaternary deformation continues along strike. With a hand level, we measured a  $1 \pm 0.5$  m high scarp across a low terrace that lies  $\sim 2$  m above the present Kashkasu River (Figures 19b and 19c). The age of the terrace and the dip of the fault are uncertain. Since the offset terrace lies below and between terraces that aggrade to moraines of the last glacial period upstream, we consider it to be postglacial in age and assume it formed 6–12 ka. The surface trace of the fault has a curved topographic expression that suggests a gentle dip. A

trapezoidal probability distribution for the dip, with maximum probability between 20 and 40°S (Appendix C), gives a dip slip rate of  $0.1 +1.1/-0.07$  mm/yr for the North Kyrkungey fault (Figure 19d). Although we saw evidence for recent surface ruptures along the fault trace, small cumulative displacement of less than a few meters across older late Quaternary surfaces (e.g., the terraces in the background of Figure 19b) suggests that the late Quaternary slip rate is low.

#### 4.5.2. South Kyrkungey Fault

[47] The South Kyrkungey fault lies 2–3 km south of and parallel to the North Kyrkungey fault (Figure 18). The fault has displaced, southeast side up, a broad terrace that is between  $\sim 40$  and 75 m above the modern Kashkasu and Bogoshti-Kakasu rivers (Figure 20a). A profile across the fault scarp shows a vertical separation of  $24 \pm 5$  m (Figure 20b). Numerous gullies along the scarp face are deflected left-laterally  $\sim 1$ –2 m, indicating a component of sinistral slip.

[48] We infer the age of the displaced terrace from stratigraphic relationships and correlation to dated terraces in other intermontane basins. Air photo analysis and field observations show that moraines inferred to be from the Last Glacial Maximum were deposited on top of a terrace

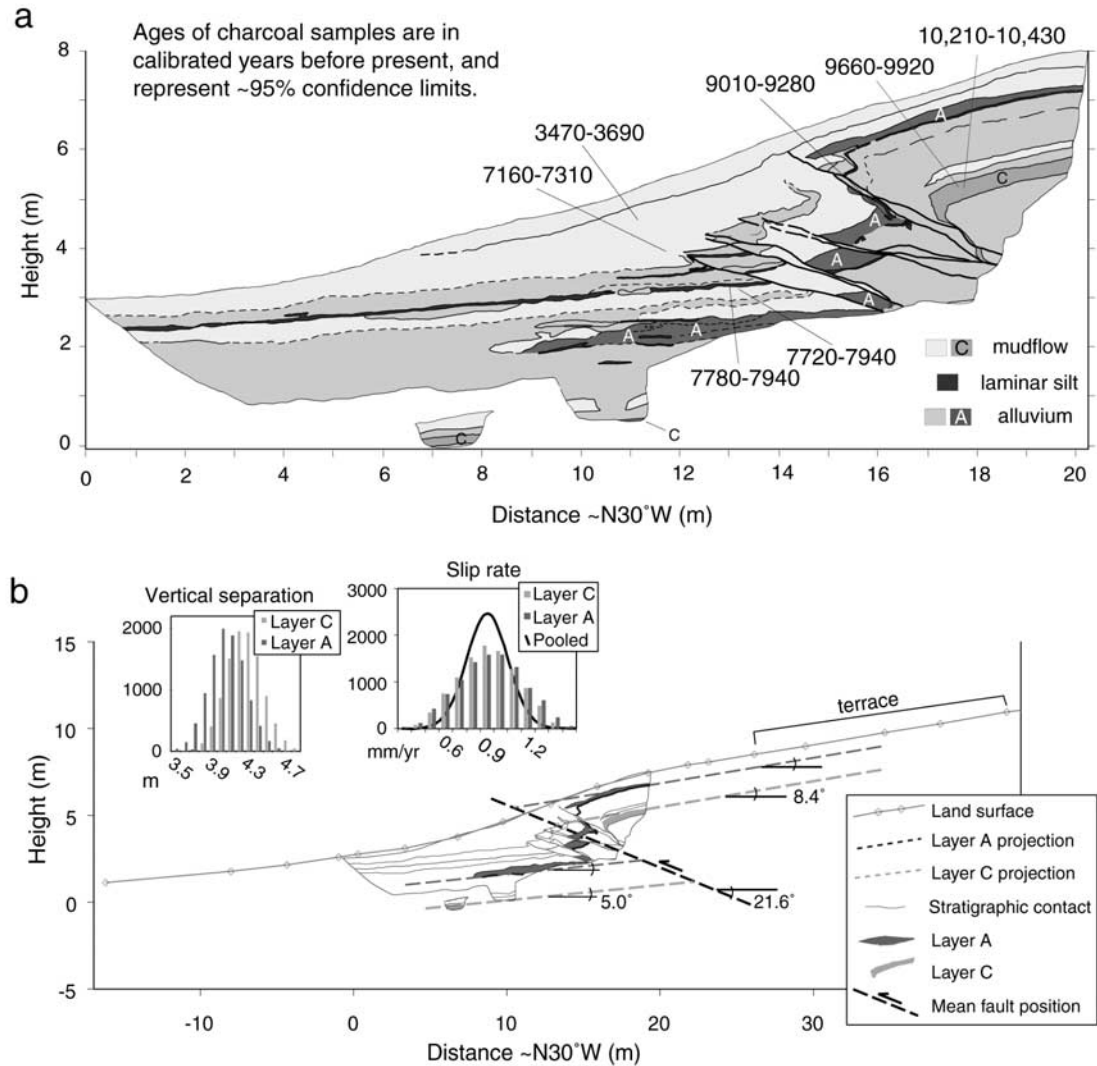


**Figure 17.** (a) Map of the west wall of the trench across the Oinak-Djar fault. We correlate layers A and C across the fault zone and use them to calculate the slip rate. (b) Profile of the land surface across the trench. To calculate slip rate, we project layers A and C into the fault zone. The slopes of the projected layers in the hanging wall are based on the dip of the terrace surface north of the trench. Changes in layer dip near the fault are interpreted to be due to drag folding. Histograms show vertical separation and slip rate using layers A and C. The line in the slip rate histogram shows the pooled mean slip rate and uncertainty by combining the two measurements.

located on the east side of the Kashkasu River that is at a height similar to the one we measured. On the basis of this stratigraphic relationship and the height and prominence of this terrace and assuming that major terraces aggraded and incised synchronously, we interpret it to be equivalent to the QII(2) terrace dated elsewhere (Figure 3 and Table 2) and assign it an age of  $141 \pm 17$  ka. On the basis of its straight map trace the fault dips steeply, and we use a trapezoidal probability distribution with maximum likelihood between  $30$  and  $70^\circ$ S (Appendix C). The parameters described above yield a rate of dip slip for the South Kyrkungey fault of  $0.2 +0.9/-0.1$  mm/yr (Figure 20b). The eastward continuation of this fault into the Kashkasu River valley does not appear to cut an inset terrace or to interrupt the same low terrace

that is cut by the North Kyrkungey fault, supporting the interpretation of a low slip rate.

## 5. Discussion

[49] We identified eight faults that appear to have the highest late Quaternary slip rates along an approximately north-south transect that crosses the northern two thirds of the central Tien Shan (Figure 21). The rates of dip-slip faulting on individual faults range from  $\sim 0.1$  to  $\sim 2.9$  mm/yr and generally accommodate shortening in a north-south direction. The high slip rates of faults within the intermontane Kochkor and Naryn basins clearly demonstrate that active shortening over the late Quaternary is distrib-

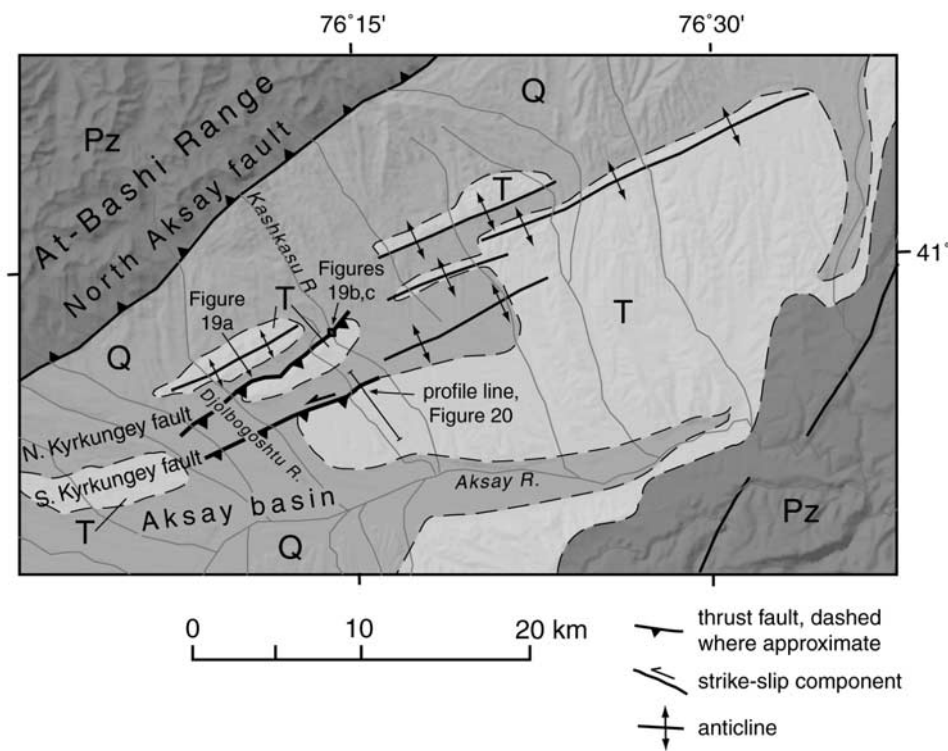


**Figure 18.** Simplified geologic map of the eastern Aksay basin. Pz, Paleozoic; T, Tertiary; Q, Quaternary. The North and South Kyrkungey faults are part of a zone of folds within the northeastern Aksay basin and appear to accommodate most of the shortening across the basin. Late Quaternary deposits include large amounts of glacial till and outwash; large moraines from the last glacial period are preserved along the southern At-Bashi Range front and are not offset by more than  $\sim 1$  m by the North Aksay fault. Locations of photos in Figure 19 and profile line in Figure 20 are shown.

uted across the belt and is not concentrated along the margins, where most historic large-magnitude earthquakes have occurred [e.g., *Molnar and Ghose*, 2000]. The most active faults lie in the major Cenozoic basins, and both the geologic mapping and pattern of terrace deformation indicate that they are active splays of fault systems that dip either north or south beneath five range/basin margins across the belt. The pattern suggests that the upper crust consists of fault-bounded blocks with a spacing of  $\sim 35$ – $80$  km.

[50] We recognize within the range blocks several Cenozoic active faults (Figure 2), indicating that deformation does occur within the range-scale “blocks.” Many of these faults lie in areas of high topography with actively eroding hillslopes and steep, bedrock-floored channels. Late Quaternary deposits and landforms that would easily record recent fault slip are few; thus, quantifying the contribution of these faults to overall mountain belt deformation is difficult. As an example, although  $\sim 200$  km of surface rupture occurred during the 1911  $M \approx 8$  Chon-Kemin earthquake [*Bogdanovitch et al.*, 1914; *Kuchai*, 1969], landslides and actively aggrading debris fans have covered much of the evidence for prior events along the portion of the fault trace that follows the narrow Chon-Kemin valley [*Delvaux et al.*, 2001].

[51] To evaluate the degree to which the faults we identified account for the total crustal shortening across the Kyrgyz central Tien Shan, we converted the calculated

fault slip rates to crustal shortening rates (Appendix D) and compared them along a transect line to modern crustal velocities measured by GPS (T. Herring and B. Hager, written communication, 2001) (Figure 21). As some of our study sites are tens of kilometers away from the transect line, we treat fault slip as constant along strike, recognizing that such an assumption cannot be correct everywhere (for example, the surface traces of the Oinak-Djar and Kyrkungey faults do not appear to extend to the transect line in Figure 21). Where we measured rates of two faults near a particular range-basin boundary, we consider the faults as splays of the same fault zone at depth and combine their shortening rates.

[52] Cumulative geologic shortening rate plotted against distance and increasing from north to south shows an approximately linear trend across the northern two thirds of the belt, with a total rate of  $11 \pm 2$  mm/yr (Figure 22). The cumulative geologic rates and current GPS rates are indistinguishable at a 95% confidence level (Figure 22). Assuming that the total rate across this area has remained constant over the past  $\sim 10^5$ – $10^6$  years and that the GPS rates are indicative of far-field convergence rates across the deforming region [cf. *Hager et al.*, 1999], slip on the faults we have studied accounts for the vast majority of crustal shortening. This result suggests that only minor deformation occurs within the blocks. The faulting and folding that do occur presently within the blocks likely resolve space problems within hanging wall material deforming differ-

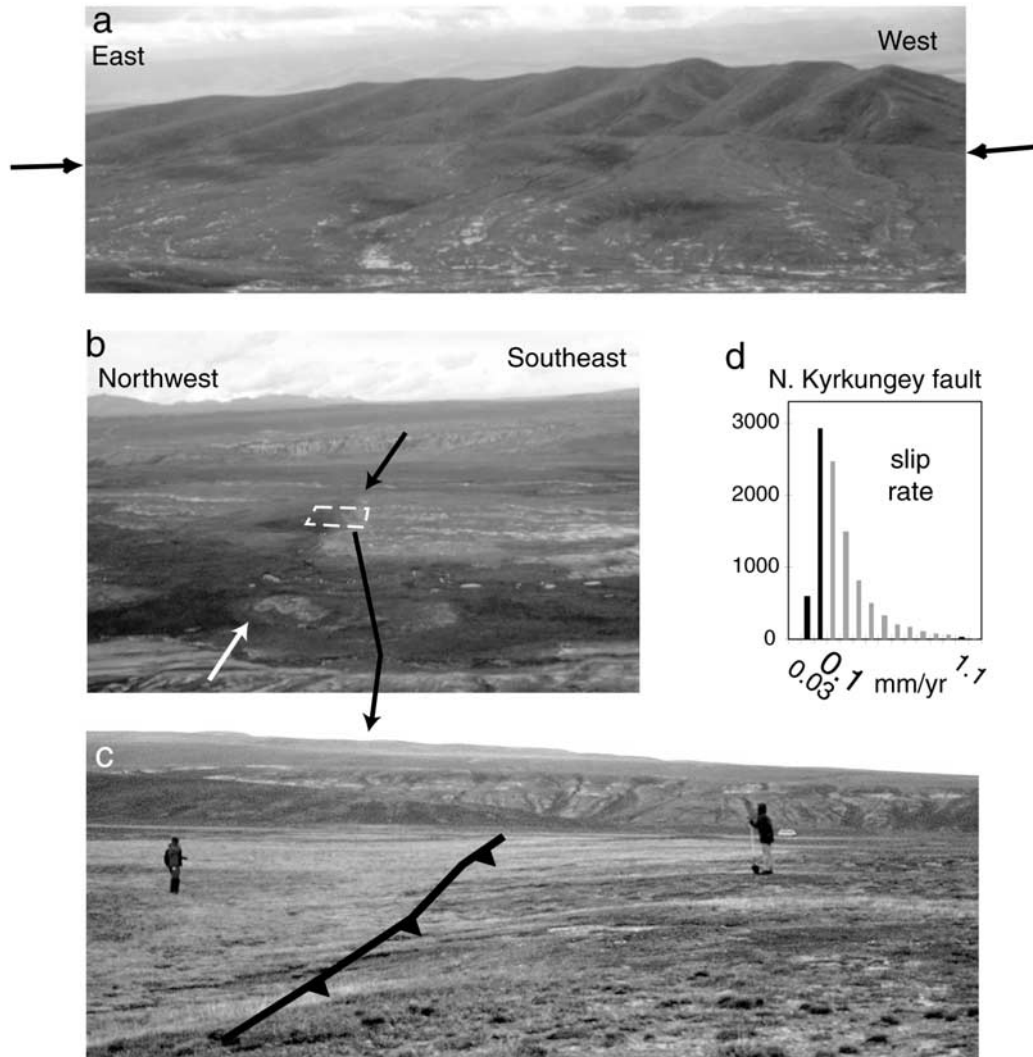


**Figure 19.** (a) View to the south of the North Kyrkungey fault scarp. The fault separates hills of Tertiary strata in the hanging wall from aggrading alluvial fans in the footwall. Although the fresh scarp morphology (between arrows) indicates recent activity, the muted morphology of the hills in the hanging wall and the lack of well-developed facets in the interfluves suggest that the fault does not have a high slip rate relative to Holocene active faults in the intermontane basins to the north. (b) View to the northeast of the contrasting vegetation and ground wetness that mark the North Kyrkungey fault (between arrows) where it crosses the floodplain of the southeastward flowing Kashkasu River. The southeast side of the fault is uplifted relative to the northwest side. (c) View to the northeast along the fault scarp (middle is marked by the fault line) across the floodplain of the Kashkasu River. Hand-level measurements across the scarp suggest a height of  $1 \pm 0.5$  m. (d) Histogram showing probability distribution of slip rate for the North Kyrkungey fault. Minimum rate is shown with an extra significant figure to distinguish it from zero.

entially across bends of major fault zones within the upper crust [Narr and Suppe, 1994].

[53] The distribution of slip rates in Figure 21 and the shortening rate profiles in Figure 22 indicate lower slip rates in the southern region, which also occupies the highest topography and thickest crust (S. Roecker, written communication, 2000). There are at least two possible explanations for the difference in an otherwise consistent strain rate pattern across the range. The first is that the crust continues to thicken beneath the high region in the south, by either

ductile flow or faulting at depth. The second is that the high topography and thick crust are nearing a limit to crustal thickening, and perhaps represent nascent plateau formation. This may be due to the extra work required to further thicken already thick crust compared to work required to thicken areas of lower mean topography, thinner crust, and lesser gravitational potential energy [e.g., Molnar and Lyon-Caen, 1988].

[54] Comparison with other regions of convergent deformation distant from plate boundaries is difficult either

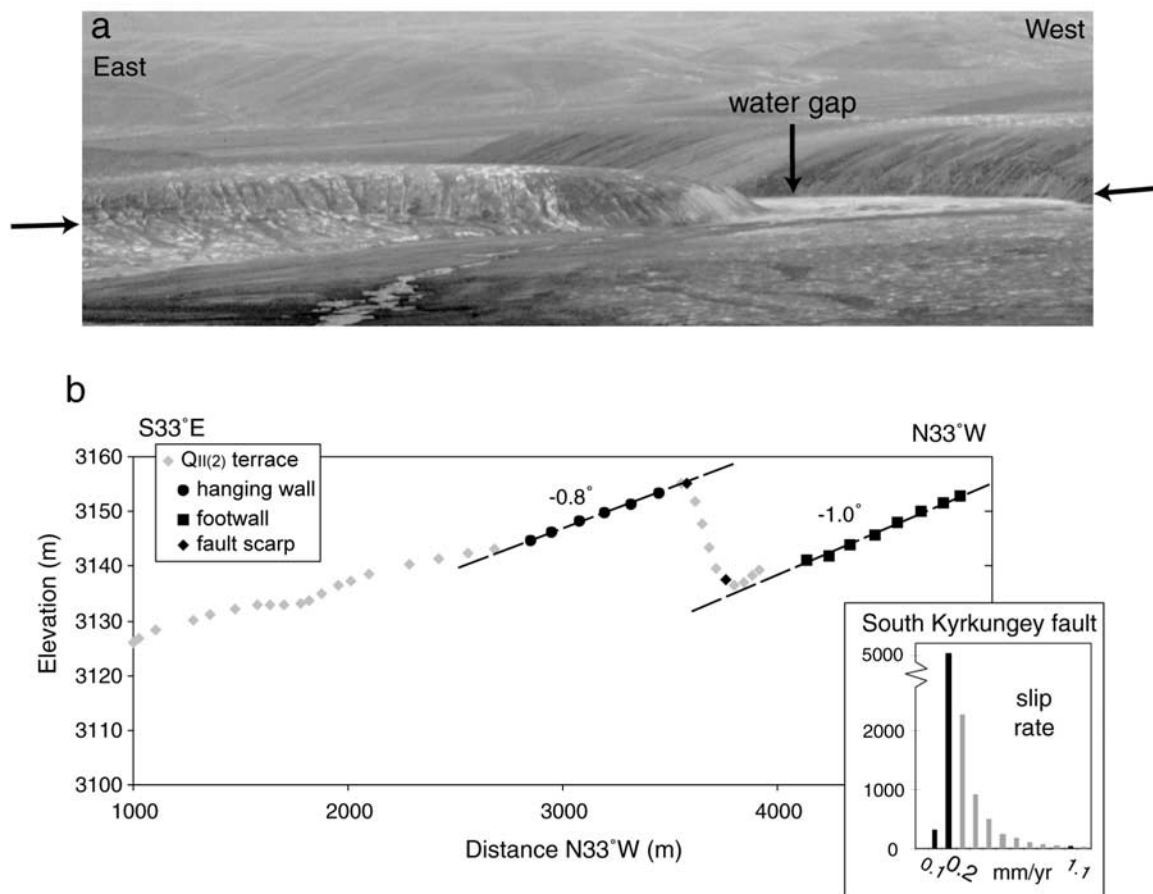


**Figure 20.** (a) View to the south of the South Kyrkungey fault. The north vergent fault here displaces the QII(2) terrace in the hanging wall against small fans and the modern floodplain of the Bogoshti-Kakasu River, which lies west of the Kashkasu River. East of the photo the older terrace is preserved in the footwall of the fault, which is the location of the topographic profile shown in Figure 20b (see also Figure 18). (b) Profile of the QII(2) terrace surface across the south dipping South Kyrkungey fault.

because other belts are ancient or because strain rate distributions have not been similarly studied. Slip across many blocks of the Rocky Mountain foreland province during the Laramide orogeny appears synchronous during the Late Cretaceous, but slip terminated at different times during the Eocene [Dickinson *et al.*, 1988]. In the Sierras Pampeanas region of Argentina, initiation appears diachronous [Coughlin *et al.*, 1998; Jordan and Allmendinger, 1986], although the numerous active range fronts showing evidence for late Quaternary or Holocene faulting indicate a currently distributed strain rate field [Costa and Vita-Finzi, 1996; Hermanns and Strecker, 1999]. A shared characteristic appears to be the geometry and spacing of deformation, with a block-like pattern of deformation with little deformation internal to the blocks [Erslev and Rogers, 1993; Gries, 1983; Hand and Sandiford, 1999; Jordan and Allmendinger, 1986].

## 6. Conclusions

[55] Our results indicate that mountain building in the Central Tien Shan occurs by concurrent slip across several

faults that span the width of the mountain belt. Active shortening occurs along the boundaries between major ranges and intermontane basins, although the most active faults penetrate and deform the intermontane basin margins. Slip rates have been distributed across the Kyrgyz Tien Shan during late Quaternary time, consistent with present-day geodetic measurements [Abdrakhmatov *et al.*, 1996] and more crudely inferred late Cenozoic rates [Abdrakhmatov *et al.*, 2001b; Makarov, 1977; Tapponnier and Molnar, 1979].

## Appendix A: Slip Rate Calculation for an Offset River Terrace

[56] We consider the case of a fault that has cut an originally planar river terrace. Our measurements are points surveyed along the terrace surface and across the fault. To calculate the amount of fault slip that has offset the terrace, we rotate and project all field data onto a vertical plane normal to the structural trend. Surveyed points from the river terrace treads define the strain markers for hanging wall and footwall deformation. Least squares linear regres-

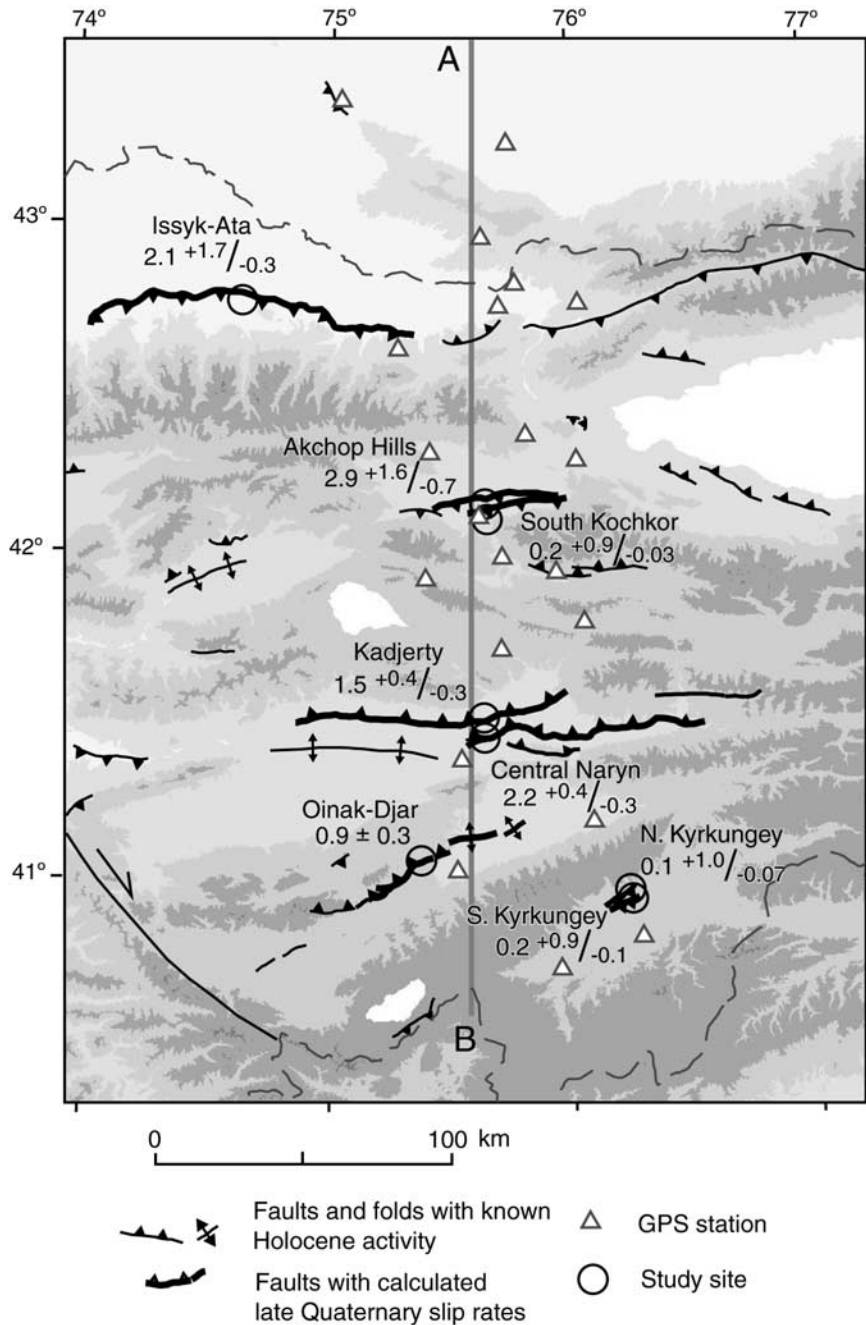


**Figure 21.** Recently active faults and fault slip rates. Gray scale changes indicate 1500-, 2500-, 3500-, and 4500-m contours. Fault names and slip rate values, in mm/yr with 95% confidence intervals, are indicated next to the study sites. The north-south components of the shortening rates are projected along fault strike to profile line A-B. Triangles show GPS stations used to compare north-south shortening rate in Figure 22.

sions of these points in an  $x$ - $y$  coordinate system determine the mean and standard error of both the slope and the intercept of the lines representing the hanging wall ( $y_h = m_h x + b_h$ ) and footwall ( $y_f = m_f x + b_f$ ), where the tangent of the terrace dip,  $\tan \alpha = m$  (Figure A1).

[57] We determine fault dip,  $\delta$ , by direct measurement, by surveying the position of the fault scarp across at least two nested terraces, or by estimation based on geomorphic expression (Appendix C). For parallel strain markers in

the hanging wall and footwall the vertical separation is  $v = b_h - b_f$ , and the dip-slip component  $s$  is

$$s = \frac{v}{\sin \delta + m \cos \delta}$$

or

$$s = \frac{v \cos \alpha}{\sin(\alpha + \delta)}. \tag{A1}$$

If the hanging wall and footwall strain marker surfaces are

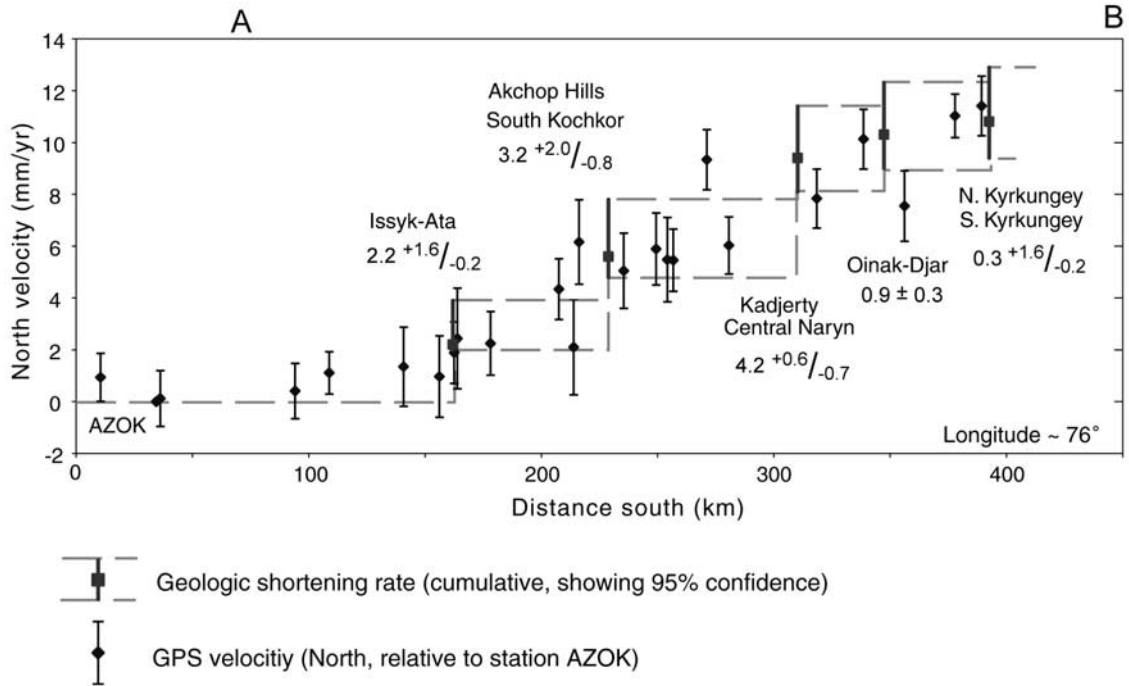


**Figure 22.** Comparison of cumulative late Quaternary geologic shortening rates and current geodetic shortening rates along a north-south transect through the Kyrgyz central Tien Shan. GPS velocities with  $2\sigma$  confidence intervals are plotted relative to station AZOK, which lies north of the mountain belt (GPS data courtesy of T. Herring and B. Hager, written communication, 2001). Geologic shortening rates of faults that are inferred to intersect at shallow depths (for example, the Akchop Hills and South Kochkor faults) are combined. Fault names and north component of shortening rate, in mm/yr with 95% confidence intervals, are indicated. Dashed lines show the 95% minimum and maximum cumulative geologic shortening rate, with vertical jumps at the faults to indicate rigid blocks separating the faults. Total north velocity and the pattern of distributed shortening rate are consistent between the data sets.

not parallel ( $m_h \neq m_f$ ), the calculated vertical separation is a function of horizontal distance

$$v(x) = x(m_h - m_f) + b_h - b_f, \quad (A2)$$

and the dip-slip calculation requires a knowledge of the position (or projection)  $P(x,y)$  of the fault tip onto the scarp (Figure A1). A line fit to the scarp face  $y = m_s x + b_s$  contains all possible points  $P$ . We divide the amount of dip

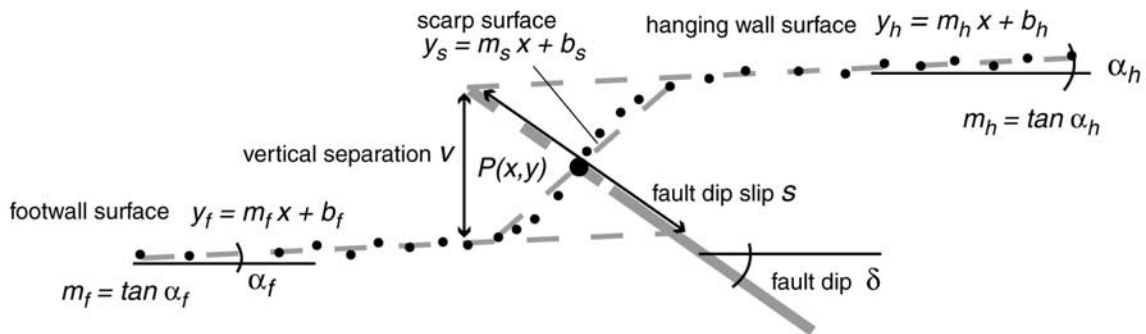


**Figure A1.** Analysis of a faulted river terrace. Surveyed points along a terrace tread that has been cut by a fault are shown. The dashed thin shaded lines indicate the hanging wall, footwall, and scarp surfaces that are represented by linear equations of the form  $y = mx + b$ , in a horizontal-vertical reference frame. The thick shaded line represents the fault and has a dashed projection updip. The scarp face and fault dip,  $\delta$ , are measured positive in opposite directions. Fault dip slip,  $s$ , depends on the position or projection of the fault within the scarp,  $P(x,y)$ , if the hanging wall and footwall slopes are different.



slip into two parts: the distance from the footwall projection up to  $P$ ,

$$s_f = \frac{x(m_s - m_f) + b_s - b_f}{\sin \delta + m_f \cos \delta} \quad (\text{A3})$$

and the distance from the hanging wall down to point  $P$ ,

$$s_h = \frac{x(m_h - m_s) + b_h - b_s}{\sin \delta + m_h \cos \delta}. \quad (\text{A4})$$

Therefore,

$$s = s_f + s_h. \quad (\text{A5})$$

Assuming that the terraces have deformed by incremental slip during earthquakes, we incorporate an additional uncertainty in slip rate due to the earthquake cycle [Sieh and Jahns, 1984]. Paleoseismic data from trench excavations suggest that major ground-rupturing earthquakes on individual faults recur on the order of one to several (1–5) thousands of years [Rubin *et al.*, 1999]. Hence deformation of a  $\sim 15$  ka terrace may have occurred during a few earthquakes. To incorporate uncertainty due to the earthquake cycle, we follow Lavé and Avouac [2000] and consider that some elastically stored slip  $\Delta s$  may be presently stored, and some elastically stored slip  $\Delta s_o$  may have been stored at the time of terrace formation. In the Monte Carlo simulations we add the additional terms  $\Delta s - \Delta s_o$  to  $s$  (Appendix C).

[58] Datable material collected from fine-grained sediments covering river terrace gravel or from within a confined deposit offset by a fault provides a measure of the time since formation of the strain marker,  $t$ . Hence the dip-slip rate,  $u$ , for the case of an offset terrace is

$$u = \frac{s + \Delta s - \Delta s_o}{t}. \quad (\text{A6})$$

## Appendix B: Measuring Slip Rate With Fault-Bend Folding of Terraces

[59] We consider the case of a terrace that has been deformed by fault-related folding, where the terrace surface is folded in the hanging wall of the fault but is buried by aggradation in the footwall. A valid geometric and kinematic interpretation of the fault-related folding must be compatible with both the terrace deformation and the underlying geologic structure. We combine measurements of deformed strata that underlie terrace treads with surveyed profiles of terrace surfaces to calculate the amount of fault slip since the terrace was formed. Our observations in the field indicate that attitudes of Tertiary beds are well approximated by kink-style geometry, with sections of relatively constant dip separated by narrow axial surfaces. The first step is to rotate a profile in the vertical plane so that axes are parallel and perpendicular to the present river gradient, which is assumed to be close to the original river gradient at the time of terrace formation. We assume that the angle between the river gradient and the fault,  $\delta$ , and the

angle between the river gradient and the hanging wall strata,  $\alpha$ , are equal (i.e., no hanging wall cut-off). Fault-bend fold theory [Suppe, 1983] is used to predict the deformation of an unconformity (i.e., terrace) above a growing fault-bend fold [Thompson *et al.*, 1999] (Figure B1).

[60] The difference in height of a terrace across a fold backlimb ( $h_1 - h_2$ ) and the fault dip beneath the terrace sections after and before the fault bend ( $\delta_1 \sim \alpha_1$  and  $\delta_2 \sim \alpha_2$ ) constrain the amount of fault dip slip  $s$  (Figure B1):

$$s = \frac{h_1 - h_2}{\sin \delta_1 - \sin \delta_2}. \quad (\text{B1})$$

A test of the fold model is possible from measurements of the dip of the terrace backlimb,  $\psi$ , defined in Figure B1:

$$\psi = \arctan \left( \frac{\sin \delta_1 - \sin \delta_2}{\cos \delta_1 + \sin \delta_2 \tan \left( \frac{\alpha_1 + \alpha_2}{2} \right)} \right). \quad (\text{B2})$$

The 95% confidence minimum and maximum, and the most probable value of slip rate are calculated using equation (A6) and the Monte Carlo simulations described in Appendix C.

[61] The fold-growth analysis also predicts the change in river height since initial floodplain abandonment and terrace formation. The difference between the height of the modern river,  $r(t)$ , and the height of the river at the time of terrace formation,  $r(t_o)$ , is

$$r(t) - r(t_o) = s^* \sin \alpha_1 - h_1. \quad (\text{B3})$$

[62] Our calculations indicate that  $r(t) - r(t_o)$ , and rates of river aggradation  $(r(t) - r(t_o))/t$ , can be significant and variable through time and that estimates of slip rate or ages of undated terraces based only on terrace height above the modern river may be significantly in error.

## Appendix C: Representation and Calculation of Uncertainties

[63] We use Monte Carlo simulations to calculate uncertainties in slip rate. Ten thousand calculations sample a variety of probability distributions that represent uncertainties for each variable (Figure C1). Frequency peaks define the most probable slip rate, and the 2.5% and 97.5% tails in the histograms bound the 95% confidence limits. These simulations take into account the standard errors associated with linear regressions of profile data ( $m$ ,  $b$ ), errors associated with measuring fault dip ( $\delta$ ), fault location across a scarp ( $P(x, y)$ ), elastic strain accumulated during the earthquake cycle ( $\Delta s$  and  $\Delta s_o$ ), and age ( $t$ ). Because the shape of the probability density function for many of the measured parameters is complex (e.g., calibrated age distributions of charcoal samples [Stuiver *et al.*, 1998]) or poorly known (e.g.,  $P(x, y)$ ), we use several methods to describe uncertainty distributions. For parameters characterized by a measurable mean and standard error (e.g.,  $m$  and  $b$ ) we use normal distributions. For parameters with either complicated (e.g.,  $t$ ) or otherwise asymmetric uncertainties, we use discrete probability distributions, which we will explain below.

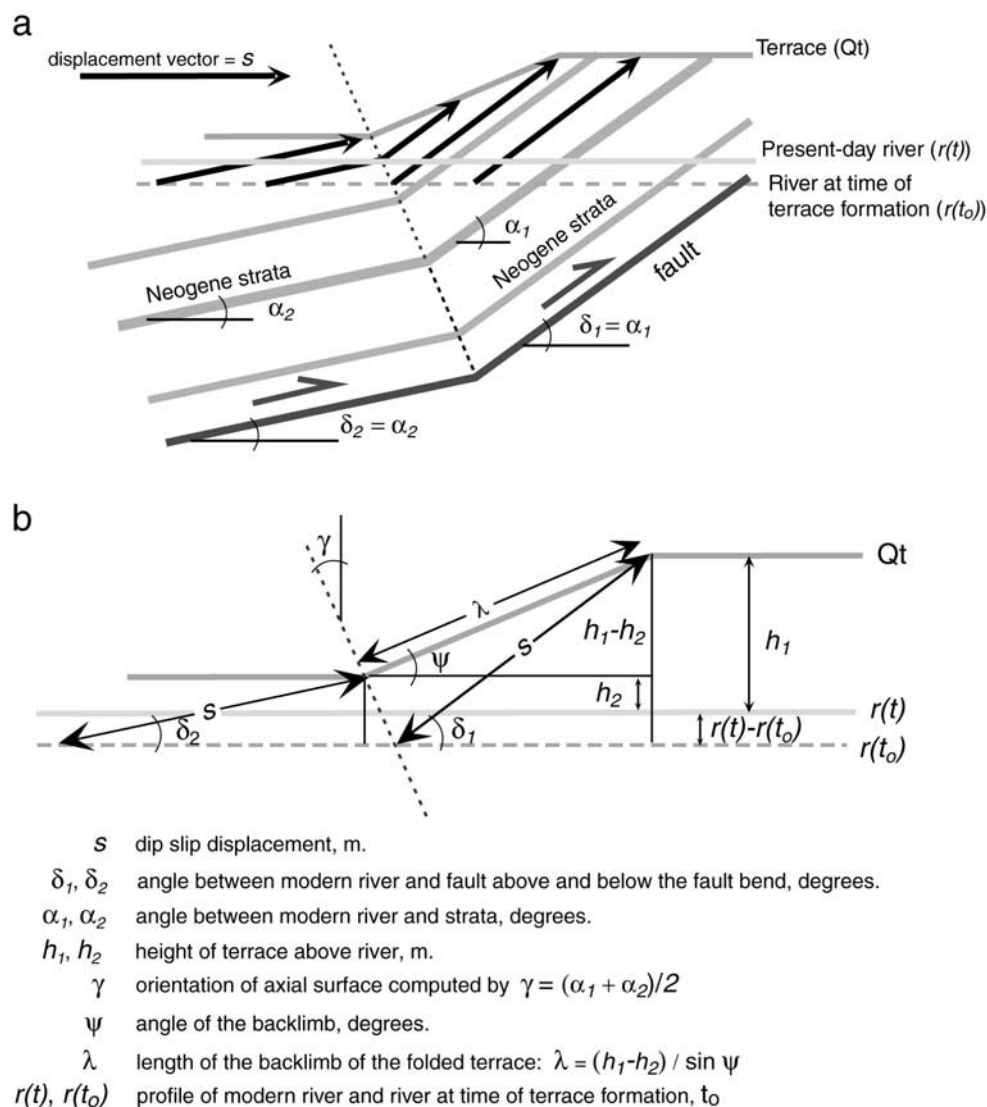


**Figure B1.** (a) Schematic illustration of terrace deformation predicted by fault-bend fold theory [Suppe, 1983]. The strath terrace is an unconformity that is displaced along with underlying layered strata that deform by slip on a fault. The diagram illustrates the case for strata oriented parallel to the underlying fault ( $\alpha = \delta$ ), an assumption we make in this study for the Issyk-Ata and Akchop Hills faults (Alamedin and Djuanarik river terraces, respectively). A constant magnitude of slip,  $s$ , occurs along the fault surface; bedding-parallel shear within the Tertiary strata accommodates slip across the fault bend. The profile of the river terrace at its time of formation,  $r(t_0)$ , is indicated by the dashed line, here shown to indicate a relative rise in river level since the time of terrace formation. (b) Parameters used to calculate dip-slip displacement,  $s$ , from the change in terrace height across a fault bend,  $h_1 - h_2$  (equation (B1)). From the measurable parameters one can also predict the relationship between the angle of the backlimb of the terrace,  $\psi$ , and the fault dips  $\delta_1$  and  $\delta_2$  (equation (B2)), and the amount of relative vertical change of the river since the terrace was formed,  $r(t) - r(t_0)$  (equation (B3)).

[64] The equations for calculating slip rate assume that strain markers that are offset by a fault (Appendix A) or that mark growth of a fold in a hanging wall (Appendix B) are planar surfaces. For deformed terraces, linear regressions of surveyed points oriented normal to fault strike provide a mean and standard error for  $m$  and  $b$  that define the strain markers. In trench exposures, linear regressions of points

that are digitized from trench logs define mean and standard error of displaced strata.

[65] Fault dip is either calculated by direct measurement, determined by cross-section geometry, or estimated based on geomorphic expression. For instances where the fault surface can be measured directly from natural and artificial exposures with an inclinometer or from a trench log, a “best

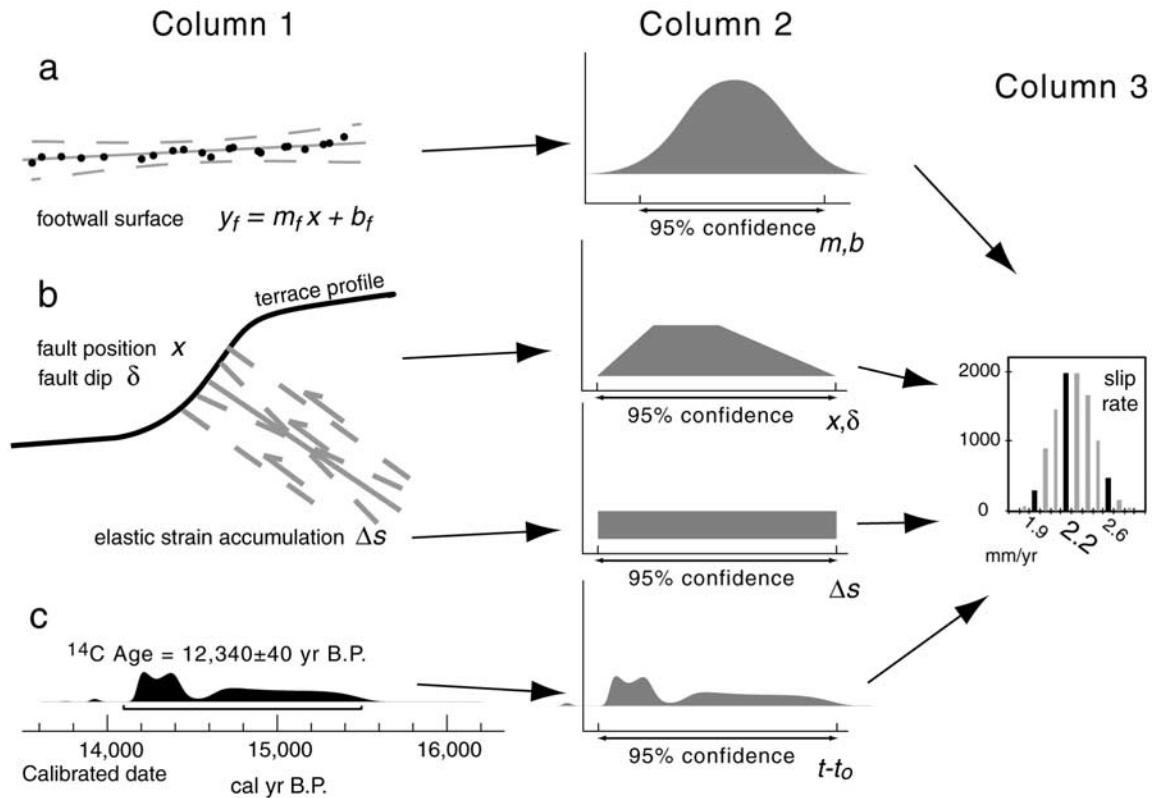


**Figure C1.** Calculation of uncertainties from measurements of slip rate variables. Column 1 indicates measurements made in the field or laboratory, and column 2 shows the probability representations of the different variables that go into the Monte Carlo simulation. (a) Linear regression of survey points on a terrace represents a hanging wall or footwall. Solid line indicates least squares fit, and dashed curved lines represent 95% confidence ranges given standard errors in slope,  $m$ , and intercept,  $b$ . (b) Measurements or constraints on the dip,  $\delta$ , and location of a fault projecting onto a scarp,  $x$ , are represented by normal, uniform, or discrete distributions. A trapezoidal distribution is shown here. Elastic strain accumulation,  $\Delta s$ , is represented by a uniform distribution. (c) Calibration of a radiocarbon age, showing probability density of calibrated ages. The discrete probability density of the calibrated age is used in the error analysis if the offset unit is constrained by one radiocarbon age. Column 3 shows an example of a histogram of slip rate. The slip rate numbers that correspond to solid histogram bars are midpoints for bins and indicate the most probable value and 95% confidence limits.

estimate” and estimated  $\sim 95\%$  confidence values are considered to equal a mean and  $2\sigma$  with a normally distributed probability distribution if the uncertainty is symmetric about the best estimate. If uncertainties are asymmetric about a best estimate, we use a triangular distribution with the best estimate having the maximum probability, and diminishing probabilities to the  $\sim 95\%$  minimum and maximum values [Humphreys and Weldon, 1994].

[66] In cases for which a fault is not directly exposed, surveying of the trends of a fault that cuts successive inset terraces allows calculation of planar fault geometry with a probability distribution based on linear regression of surveyed points. For faults that are blind or buried and fault slip is manifested by growth of a fold, fault dip is derived from measurements of strata exposed within the hanging wall and fault-related fold models of fold growth [Suppe, 1983]. In the two cases we show in this paper, we use cross-section solutions that assume faults locally cut parallel to hanging wall strata [e.g., Lavé and Avouac, 2000], and the measurements of hanging wall strata ( $\alpha$ , the angle between

the strata and the modern river profile) determine the mean and standard deviation of the fault angle ( $\delta$ , the angle between the fault and the modern river profile).

[67] In cases for which direct measurement of the fault dip was not possible or hanging wall strata were unexposed or ambiguously related to fault orientation, we estimate fault dip based on topographic expression and by analogy with other faults in similar physiographic settings. Faults that appear to dip steeply are represented by a trapezoidal probability distribution, with an equal and maximum likelihood between  $30^\circ$  and  $70^\circ$  and probabilities diminishing linearly to zero at  $0^\circ$  and  $90^\circ$  dips. Faults that appear to dip shallowly have a trapezoidal distribution with equal and maximum likelihood between  $20^\circ$  and  $40^\circ$  and probabilities diminishing linearly to zero at  $0^\circ$  and  $90^\circ$  dips.

[68] If the position (or projection) of the fault within the fault scarp ( $P(x, y)$ ) is unknown, we use a trapezoidal probability distribution to represent  $x$  in equations (A2)–(A4). On the basis of examples of exposed thrust faults in our study area and reviews in the literature [Carver and McCalpin,

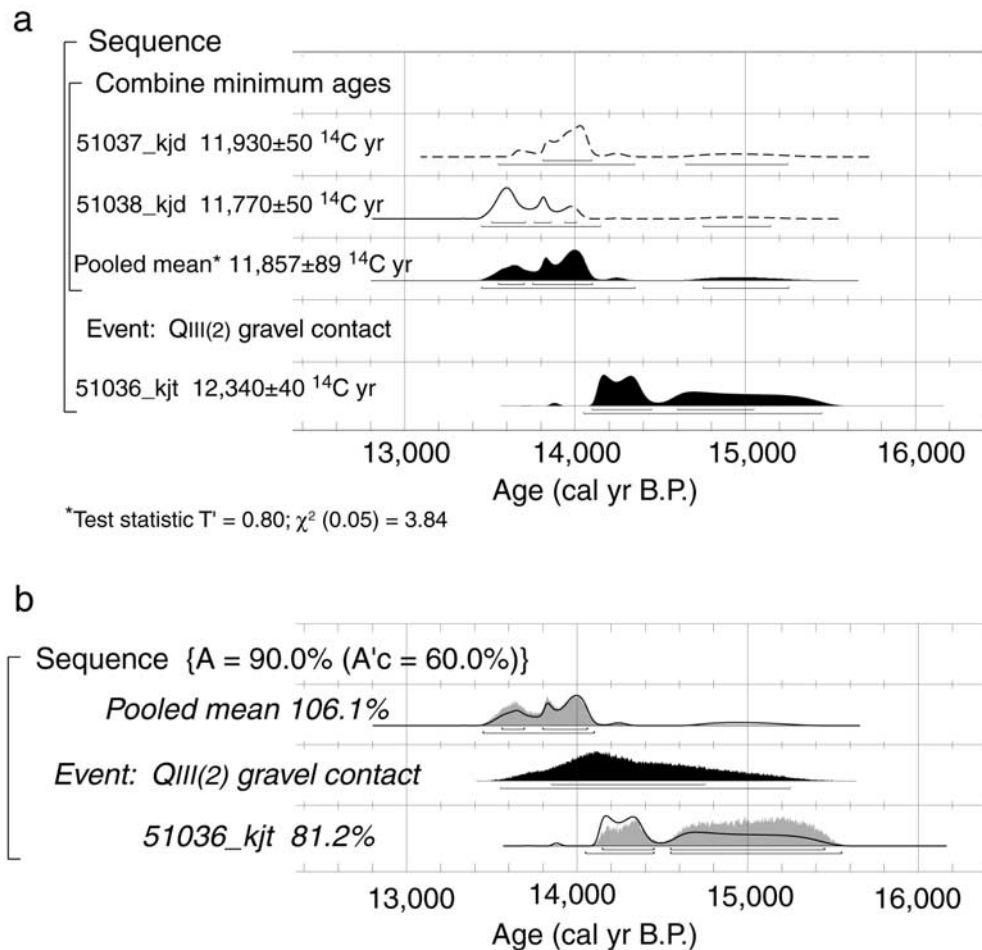


**Figure C2.** Age analysis of the QIII(2) terrace at the Kadjerty River, Naryn basin, using the program OxCal 3.5 [Ramsey, 1995]. The goal is to statistically describe the age distribution of the terrace forming “event,” which is represented by the contact between coarse gravel and overlying silt and sand. (a) Radiocarbon sample ages and calibrated age distributions for three detrital charcoal samples. Overlying the event is the calibrated age distribution of the pooled mean radiocarbon age of two statistically similar detrital charcoal samples collected from above the gravel contact (similarity test described by Ward and Wilson [1978]). Calibrated ages of the individual charcoal samples are shown by dashed lines. Underlying the event is the calibrated age of the charcoal sample collected below the gravel contact. (b) Age analysis of the event using Bayesian statistical methods described by Ramsey [1998]. The calibrated age distributions of the original samples above and below the event are indicated by solid lines. Shaded area indicates the reweighted age distribution based on the additional constraint of stratigraphic order. The a posteriori age distribution of the event is determined from the reweighted distributions of the sample ages and an unconstrained a priori distribution of the event. The agreement index indicates the extent to which the final (a posteriori) sample age distribution overlaps with the original (a priori) sample distribution. Index values below 60% are questionable (this level of disagreement is very similar to that for the 5% level chi-square test). In this example, the overall agreement index  $A$  exceeds the critical agreement  $A'c$ .

1996], we give a maximum probability to a fault that projects to  $1/3 - 1/2$  the distance along the scarp face measured from the base of the fault scarp and a likelihood diminishing to zero at the top and base of the scarp.

[69] For uncertainties associated with the earthquake cycle we follow Lavé and Avouac [2000] and consider that some elastically stored slip  $\delta s$  may be presently stored, and some elastically stored slip  $\delta s_o$  may have been stored at the time of terrace formation. In the Monte Carlo simulations we add the additional term  $\Delta s - \Delta s_o$  to  $s$  and assume that

the values  $\Delta s$  and  $\Delta s_o$  range uniformly between zero and a maximum of 5 m, a value slightly greater than the maximum 4.2 m surface fault slip caused by the 1992  $M_s$  7.3 Suusamyр earthquake [Ghose *et al.*, 1997]. In instances where a scarp appears to have formed in a single earthquake, we limit  $\Delta s$  and  $\Delta s_o$  to vary between zero and the calculated value of  $s$ .

[70] We use a variety of methods to generate probability distributions for the ages of strain markers in our slip rate calculations. Because of fluctuations in cosmogenically

produced atmospheric  $^{14}\text{C}$  through time, radiocarbon ages of organic material that incorporate atmospheric  $^{14}\text{C}$  require calibration in order to be converted to the calendric timescale [Stuiver and Reimer, 1986; Stuiver et al., 1998]. Calibration programs [Ramsey, 1995; Stuiver and Reimer, 1986] use published calibration curves [Stuiver et al., 1998] to convert radiocarbon ages and analytical uncertainties to calibrated (approximately calendric) dates with discrete probability distributions (Figure 3 and Table 1). Although detrital charcoal within a deposit has an inherited age that is older than the age of deposition, we presume that this inherited age is negligible compared to the analytical uncertainty of the radiocarbon age (typically 40–80  $^{14}\text{C}$  yr for our samples, see Table 1). In cases where the age of a deposit is constrained by a single radiocarbon sample (e.g., a charcoal sample collected from an offset layer in a trench), we use the discrete probability distribution of the calibrated radiocarbon age in our slip rate calculations (Figure C1c). If more than one sample is collected from a deposit, a significance test determines whether the pooled mean radiocarbon age is calibrated to determine the unit age [Stuiver and Reimer, 1986] or a combined and reweighted probability distribution is used for the age [e.g., Biasi and Weldon, 1994].

[71] In cases for which the age of a contact is desired (e.g., the geologic event that is the paleo-river incision and terrace formation, approximately represented by the contact between river gravel and overlying fine-grained sediments), and samples collected from above and below the contact constrain its age, the extra condition of stratigraphic order is used to reweight the calibrated age distributions to generate a discrete probability distribution for the age of the contact [Biasi and Weldon, 1994; Ramsey, 1998]. For example, three radiocarbon dates on detrital charcoal constrain the age of river incision, floodplain abandonment, and formation of the QIII(2) terrace along the Kadjerty River (Figure 3 and Table 1). The pooled mean radiocarbon age of two charcoal samples collected in sandy silt 10 and 30 cm above the upper gravel contact in a gully exposure  $\sim 2$  km south of the fault scarp (Figures 11 and 12c) yields a calibrated radiocarbon age of  $13.5\text{--}14.1 \times 10^3$  cal years B.P. (Table 1). A charcoal sample collected 10 cm below the upper gravel contact in an exposure across the fault scarp (Figures 11 and 12b) has an age of  $\sim 14.1\text{--}15.4 \times 10^3$  yr cal years B.P. (Table 1). Assuming that the charcoal samples closely date the deposits and that the contact between the gravel and overlying sandy silt represents the incision of the paleoriver and formation of the QIII(2) terrace, the extra condition of stratigraphic superposition changes the probability distribution of the age of the contact (Figure C2).

[72] Although the TL and IRSL ages of the QII(2) terraces have large uncertainties (Figure 3 and Table 2) and the samples collected from fine-grained sediments overlying river gravel represent minimum ages for the terraces, statistical tests of significance [Ward and Wilson, 1978] cannot reject the hypothesis that all of the QII(2) ages come from the same population (test statistic  $T = 2.51$ ;  $\chi^2(0.05) = 7.81$ ). To increase the precision for the slip rate calculations based on deformed QII(2) terraces, we use the pooled mean age (140.7 ka) and standard deviation (square root of the variance of the pooled ages, 8.5 ka) of the statistically similar TL/IRSL analyses. In the text we report the mean and  $\sim 95\%$  confidence interval as  $141 \pm 17$  ka.

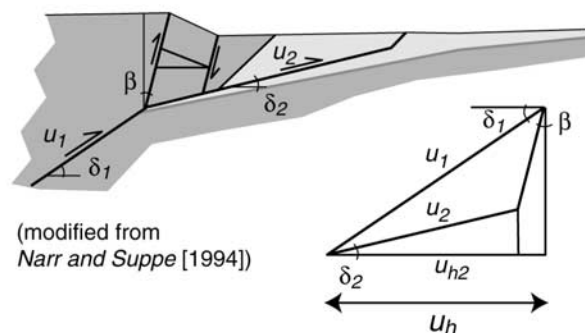


**Figure D1.** Conversion from fault slip rate to horizontal shortening rate. Following the kinematics proposed by Narr and Suppe [1994], we assume that slip across a fault bend is accommodated by hanging wall shear of angle  $\beta$ , measured from vertical. If  $\beta = 0$ , the horizontal shortening rate,  $u_h$ , equals the slip rate on the fault above the bend,  $u_2$ , times the cosine of the fault dip,  $\delta_2$ . If  $\beta \neq 0$ ,  $u_h$  is a function of  $\beta$  and the dip of the fault below the bend,  $\delta_1$  (equation (D1)).

[73] For the study sites where we do not have local age control (e.g., in the southernmost Aksay basin) we use geomorphic criteria and correlation to estimate terrace ages. For terraces mapped as QII(2) or QIII(2) we use the pooled mean age of the terrace determined at other sites.

#### Appendix D: Converting Slip Rates to Geologic Shortening Rates

[74] To convert the slip rate on a fault to its contribution to the shortening rate across the region, we cannot assume that slip on the crustal-scale ramp equals that on the fault segments at shallow crustal depths (Figure D1). Most of the faults that we have examined in this study dip  $\sim 20\text{--}40^\circ$  at the surface and appear to flatten to dips of  $\sim 5\text{--}20^\circ$  at depths of less than a few kilometers, within Tertiary sedimentary rock (e.g., Figures 9 and B1). Fault-bend fold theory predicts that in layered strata at least, where shear can occur parallel to bedding, slip on consecutive fault segments with dips that steepen upward remains approximately constant [see Suppe, 1983, p. 699].

[75] The shallow faults that lie at a few kilometers depth appear to intersect more steeply dipping faults that underlie the mountain ranges and to involve much of the previously deformed basement rock in the upper crust [e.g., Avouac et al., 1993; Burchfiel et al., 1999]. Strain must occur in the hanging wall to absorb the movement in different directions of the portions adjacent to segments with different dips. The fraction of slip,  $s$ , transferred from a deeper, steeper fault (dip =  $\delta_1$ ) to a more gently dipping, shallower fault (dip =  $\delta_2$ ) is approximately equal to  $\cos\delta_1/\cos\delta_2$  (see the fault-bend anticline example of Narr and Suppe [1994, p. 814] and Figure D1). Where deformation of the hanging wall occurs only by shear on vertical planes, the approximate equality becomes exact. In the case where shear occurs on planes with a nonzero angle  $\beta$ , the equation for the shortening rate  $u_h$ , is

$$u_h = \frac{u_2 \cos \delta_2 (1 - \tan \delta_2 \tan \beta)}{1 - \tan \delta_1 \tan \beta}. \quad (\text{D1})$$

Values of  $u_2$  are derived from our slip calculations, and we estimate (or infer)  $\delta_2$  from cross sections and folds in terrace profiles. Where we have no mapping constraints on  $\delta_2$ , we allow it to vary between the dip of the fault measured or estimated at the surface in our slip rate calculations and  $0^\circ$ . For  $\delta_1$  we assume that crustal scale ramps dip between  $\delta_2$  and  $55^\circ$  (the maximum dip of the intermontane 1992 Susamyr earthquake [Mellors *et al.*, 1997]), and we assign  $\beta$  values between  $0$  and  $5^\circ$ .

[76] We compare our late Quaternary shortening rates to the north component of GPS shortening rates. In order to resolve geologic shortening into its north-south component,  $u_{N-S}$ , we assume pure dip slip on each fault ( $u_{N-S} \leq u_h$ ) or assume that oblique slip occurs such that maximum shortening is oriented N-S ( $u_{N-S} \geq u_h$ ). We incorporate this uncertainty by defining  $\phi$  as the angle between the strike-normal direction of the fault and north and assuming:

$$u_h \cos \phi \leq u_{N-S} \leq u_h / \cos \phi. \quad (D2)$$

[77] **Acknowledgments.** The scientific station IVTAN, under the leadership of the late Y. A. Trapeznikov and G. Schletchkov, provided excellent logistical support in the field. We thank K. Armstrong, M. Bullen, D. Burbank, K. Fengler, J. Lavé, K. McLean, M. Miller, K. Weberling, and C. Whitehill for help in the field and Atyr Abdrakhmatov for excellent cooking. T. Herring and B. Hager provided GPS velocities prior to publication. Reviews of an earlier version by B. Atwater and A. Gillespie, and formal reviews by Associate Editor Jeff Freymueller and an anonymous reviewer improved the manuscript. This work was supported in part by NSF research grant EAR 96-14412 and by grants from the Geological Society of America, American Association of Petroleum Geologists, and the University of Washington Department of Geological Sciences to Thompson.

## References

- Abdrakhmatov, K. Y., *Quaternary Tectonics of the Chu Basin* (in Russian), 120 pp., Ilim, Bishkek, Kyrgyzstan, 1988.
- Abdrakhmatov, K. Y., et al., Relatively recent construction of the Tien Shan inferred from GPS measurements of present-day crustal deformation rates, *Nature*, 384(6608), 450–453, 1996.
- Abdrakhmatov, K. Y., S. Thompson, R. Weldon, D. Delvaux, and J. Klerkx, Active faults of Tien-Shan (in Russian), *Nauka Novye Tehnol.*, 2, 22–28, 2001a.
- Abdrakhmatov, K. Y., R. J. Weldon, S. C. Thompson, D. W. Burbank, C. M. Rubin, M. M. Miller, and P. Molnar, Onset, style, and current rate of shortening in the central Tien Shan, Kyrgyz Republic (in Russian), *Geol. Geofiz.*, 42, 1585–1609, 2001b.
- Aitken, M. J., *Thermoluminescence Dating*, 359 pp., Academic, San Diego, Calif., 1985.
- Aitken, M. J., *Introduction to Optical Dating*, 256 pp., Oxford Univ. Press, New York, 1998.
- Avouac, J. P., P. Tapponnier, M. Bai, H. You, and G. Wang, Active thrusting and folding along the northern Tien Shan and late Cenozoic rotation of the Tarim relative to Dzungaria and Kazakhstan, *J. Geophys. Res.*, 98, 6755–6804, 1993.
- Bally, A. W., L. Burbi, C. Cooper, and R. Ghelardoni, Balanced sections and seismic reflection profiles across the central Apennines, *Mem. Soc. Geol. It.*, 35, 257–310, 1986.
- Benedetti, L., P. Tapponnier, G. C. P. King, B. Meyer, and I. Manighetti, Growth folding and active thrusting in the Montello region, Veneto, northern Italy, *J. Geophys. Res.*, 105, 739–766, 2000.
- Berger, G. W., Dating Quaternary events by luminescence, in *Dating Quaternary Sediments*, edited by D. J. Easterbrook, *Spec. Pap. Geol. Soc. Am.*, 227, 13–50, 1988.
- Berger, G. W., Effectiveness of natural zeroing of the thermoluminescence in sediments, *J. Geophys. Res.*, 95, 12,375–12,397, 1990.
- Berger, G. W., R. A. Lockhart, and J. Kuo, Regression and error analysis applied to the dose-response curves in thermoluminescence dating, *Nucl. Tracks Radiat. Meas.*, 13, 177–184, 1987.
- Biasi, G. P., and R. J. Weldon, Quantitative refinement of calibrated 14C distributions, *Quat. Res.*, 41, 1–18, 1994.
- Bogdanovitch, K. I., I. M. Kark, B. Y. Korolkov, and D. I. Mushketov, *The Earthquake in the Northern Districts of the Tien Shan, 22 December 1910 (4 January 1911)* (in Russian), Comm. of the Geol. Comm., St. Petersburg, Russia, 1914.
- Boyer, S. E., Geometric evidence for synchronous thrusting in the southern Alberta and northwest Montana thrust belts, in *Thrust Tectonics*, edited by K. R. McClay, pp. 377–390, Chapman and Hall, New York, 1992.
- Boyer, S. E., and D. Elliott, Thrust systems, *AAPG Bull.*, 66, 1196–1230, 1982.
- Brown, E. T., D. L. Bourles, B. C. Burchfiel, Q. Deng, J. Li, P. Molnar, G. M. Raisbeck, and F. You, Estimation of slip rates in the southern Tien Shan using cosmic ray exposure dates of abandoned alluvial fans, *Geol. Soc. Am. Bull.*, 110, 377–386, 1998.
- Bullen, M. E., D. W. Burbank, J. I. Garver, and K. Y. Abdrakhmatov, Late Cenozoic tectonic evolution of the northwestern Tien Shan: New age estimates for the initiation of mountain building, *Geol. Soc. Am. Bull.*, 113, 1544–1559, 2001.
- Burbank, D. W., J. K. McLean, M. Bullen, K. Y. Abdrakhmatov, and M. M. Miller, Partitioning of intermontane basins by thrust-related folding, Tien Shan, Kyrgyzstan, *Basin Res.*, 11, 75–92, 1999.
- Burchfiel, B. C., E. T. Brown, Q. Deng, X. Feng, J. Li, P. Molnar, J. Shi, Z. Wu, and H. You, Crustal shortening on the margins of the Tien Shan, Xinjiang, China, *Int. Geol. Rev.*, 41, 665–700, 1999.
- Burtman, V. S., *The Talaso-Ferghana Strike-Slip Fault* (in Russian), 143 pp., Nauka, Moscow, 1964.
- Burtman, V. S., Structural geology of Variscan Tien Shan, USSR, *Am. J. Sci.*, 275-A, 157–186, 1975.
- Burtman, V. S., S. F. Skobelev, and P. Molnar, Late Cenozoic slip on the Talas-Ferghana Fault, the Tien Shan, Central Asia, *Geol. Soc. Am. Bull.*, 108, 1004–1021, 1996.
- Butler, R. W. H., Thrust tectonics, deep structure and crustal subduction in the Alps and Himalayas, *J. Geol. Soc. London*, 143(6), 857–873, 1986.
- Carver, G. A., and J. P. McCalpin, Paleoseismology of compressional tectonic environments, in *Paleoseismology*, edited by J. P. McCalpin, pp. 183–270, Academic, San Diego, Calif., 1996.
- Chediya, O. K., *Morphology and Neotectonics of the Tien Shan* (in Russian), 313 pp., Ilim, Bishkek, Kyrgyzstan, 1986.
- Cobbold, P. R., E. Sadybakasov, and J. C. Thomas, Cenozoic transpression and basin development, Kyrgyz Tien Shan, central Asia, in *Geodynamic Evolution of Sedimentary Basins, International Symposium*, edited by N. E. F. Roure, V. S. Shein, and I. Skvortsov, pp. 181–202, Technip, Paris, 1994.
- Cook, F. A., D. S. Albaugh, L. D. Brown, S. Kaufman, J. E. Oliver, and R. D. J. Hatcher, Thin-skinned tectonics in the crystalline southern Appalachians; COCORP seismic-reflection profiling of the Blue Ridge and Piedmont, *Geology*, 7(12), 563–567, 1979.
- Costa, C. H., and C. Vita-Finzi, Late Holocene faulting in the southeast Sierras Pampeanas of Argentina, *Geology*, 24(12), 1127–1130, 1996.
- Coughlin, T. J., P. B. O'Sullivan, B. P. Kohn, and R. J. Holcombe, Apatite fission-track thermochronology of the Sierras Pampeanas, central western Argentina; implications for the mechanism of plateau uplift in the Andes, *Geology*, 26(11), 999–1002, 1998.
- Dahlen, F. A., Noncohesive critical Coulomb wedges: An exact solution, *J. Geophys. Res.*, 89, 10,125–10,133, 1984.
- Dahlstrom, C. D. A., Structural geology in the eastern margin of the Canadian Rocky Mountains, *Bull. Can. Pet. Geol.*, 18, 332–406, 1970.
- Davis, D., J. Suppe, and F. A. Dahlen, Mechanics of fold-and-thrust belts and accretionary wedges, *J. Geophys. Res.*, 88, 1153–1172, 1983.
- Delvaux, D., K. Y. Abdrakhmatov, and J. Klerkx, The South Kemin fault and evidence for earthquakes prior to the 1911 event, Kyrgyz Republic (in Russian), *Geol. Geofiz.*, 42, 1667–1677, 2001.
- DeMets, C., R. G. Gordon, D. F. Argus, and S. Stein, Effect of recent revisions to the geomagnetic reversal time scale on estimates of current plate motions, *Geophys. Res. Lett.*, 21, 2191–2194, 1994.
- Dickinson, W. R., M. A. Klute, M. J. Hayes, S. U. Jancek, E. R. Lundin, M. A. McKittrick, and M. D. Olivares, Paleogeographic and paleotectonic setting of Laramide sedimentary basins in the central Rocky Mountain region, *Geol. Soc. Am. Bull.*, 100, 1023–1039, 1988.
- Erslev, E. A., and J. L. Rogers, Basement-cover geometry of Laramide fault-propagation folds, in *Laramide Basement Deformation in the Rocky Mountain Foreland of the Western United States*, edited by C. J. Schmidt, R. B. Chase, and E. A. Erslev, pp. 125–146, Geol. Soc. of Am., Boulder, Colo., 1993.
- Fairbanks, R. G., A 17,000 year glacio-eustatic sea level record: Influence of glacial melting rates on the Younger Dryas event and deep-ocean circulation, *Nature*, 345, 637–642, 1989.

- Fedorovich, B. A., *Data of Geology and Geochemistry of the Tien Shan* (in Russian), 243 pp., Acad. of Sci. of USSR, Moscow, 1935.
- Ghose, S., R. J. Mellors, A. M. Korjenkov, M. W. Hamburger, T. L. Pavlis, G. L. Pavlis, M. Omuraliev, E. Mamyrov, and A. R. Muraliev, The  $M_s = 7.3$  1992 Suusamy, Kyrgyzstan, earthquake in the Tien Shan, 2, After-shock focal mechanisms and surface deformation, *Bull. Seismol. Soc. Am.*, 87, 23–38, 1997.
- Ghose, S., M. W. Hamburger, and C. Ammon, Source parameters of moderate-size earthquakes in the Tien Shan, central Asia from regional movement tensor inversion, *Geophys. Res. Lett.*, 25, 3181–3184, 1998.
- Gillespie, A. R., and P. Molnar, Asynchronous maximum advances of mountain and continental glaciers, *Rev. Geophys.*, 33(3), 311–364, 1995.
- Gries, R. R., Oil and gas prospecting beneath Precambrian of foreland thrust plates in Rocky Mountains, *AAPG Bull.*, 67(1), 1–28, 1983.
- Grigorienko, P. G., The main features of geological development of Krygyz Tien Shan during the Quaternary Period (in Russian), in *Materials About Cenozoic Geology and the Newest Tectonics of the Tien Shan*, pp. 3–11, Ilim, Bishkek, Kyrgyzstan, 1970.
- Hager, B. H., G. A. Lyzenga, A. Donnellan, and D. Danan, Reconciling rapid strain accumulation with deep seismogenic fault planes in the Ventura basin, California, *J. Geophys. Res.*, 104, 25,207–25,219, 1999.
- Hand, M., and M. Sandiford, Intraplate deformation in central Australia, the link between subsidence and fault reactivation, *Tectonophysics*, 305, 121–140, 1999.
- Henderson, G. M., and N. C. Slowey, Evidence from U-Th dating against Northern Hemisphere forcing of the penultimate deglaciation, *Nature*, 404, 61–66, 2000.
- Hermanns, R. L., and M. R. Strecker, Structural and lithological controls on large Quaternary rock avalanches (sturzstroms) in arid northwestern Argentina, *Geol. Soc. Am. Bull.*, 111, 934–948, 1999.
- Holt, W. E., R. N. Chamot, X. Le-Pichon, A. J. Haines, T. B. Shen, and J. Ren, Velocity field in Asia inferred from Quaternary fault slip rates and Global Positioning System observations, *J. Geophys. Res.*, 105, 19,185–19,209, 2000.
- Humphreys, E. D., and R. J. I. Weldon, Deformation across the western United States: A local estimate of Pacific–North America transform deformation, *J. Geophys. Res.*, 99, 19,975–20,010, 1994.
- Ikeda, Y., Thrust-front migration and its mechanism; evolution of intraplate thrust fault system, *Bull. Dep. Geogr. Univ. Tokyo*, 15, 125–159, 1983.
- Imbrie, J., J. D. Hays, D. G. Martinson, A. McIntyre, A. C. Mix, J. J. Morley, N. G. Pisias, W. L. Prell, and N. J. Shackleton, The orbital of Pleistocene climate: Support from a revised chronology of the marine  $^{18}\text{O}$  record, in *Milankovitch and Climate*, edited by A. L. Berger, pp. 269–305, D. Reidel, Norwell, Mass., 1984.
- Jordan, T. E., and R. W. Allmendinger, The Sierras Pampeanas of Argentina: A modern analogue of Rocky Mountain foreland deformation, *Am. J. Sci.*, 286, 737–764, 1986.
- Knauf, V. I., Tectonic zoning of northern Kyrgyzia (in Russian), *Geotectonica*, 5, 48–54, 1976.
- Koyi, H. A., K. Hessami, and A. Teixell, Epicenter distribution and magnitude of earthquakes in fold-thrust belts: insights from sandbox models, *Geophys. Res. Lett.*, 27, 273–276, 2000.
- Kuchai, V. K., Results of repeated examination of the remaining deformation in the pleistoseist of the Kebin earthquake (in Russian), *Geol. Geofiz.*, 101–108, 1969.
- Lavé, J., and J. P. Avouac, Active folding of fluvial terraces across the Siwaliks Hills, Himalayas of central Nepal, *J. Geophys. Res.*, 105, 5735–5770, 2000.
- Le Fort, P., Himalayas: The collided range. Present knowledge of the continental arc, *Am. J. Sci.*, 275-A, 1–44, 1975.
- Makarov, V. I., *New Tectonic Structures of the Central Tien Shan* (in Russian), 171 pp., Order of the Red Banner Geol., Inst., Akad. of Sci., Moscow, 1977.
- Mattauer, M., Sur le mécanisme de formation de la schistosité dans l'Himalaya, *Earth Planet. Sci. Lett.*, 28, 144–154, 1975.
- Mellors, R. J., F. L. Vernon, G. L. Pavlis, G. A. Abers, M. W. Hamburger, S. Ghose, and B. Iliasov, The  $M_s = 7.3$  1992 Suusamy, Kyrgyzstan, earthquake, 1, Constraints on fault geometry and source parameters based on aftershocks and body-wave modeling, *Bull. Seismol. Soc. Am.*, 87, 11–22, 1997.
- Merritts, D. J., K. R. Vincent, and E. E. Wohl, Long river profiles, tectonism, and eustasy: A guide to interpreting fluvial terraces, *J. Geophys. Res.*, 99, 14,031–14,050, 1994.
- Molnar, P., and S. Ghose, Seismic moments of major earthquakes and the rate of shortening across the Tien Shan, *Geophys. Res. Lett.*, 27, 2377–2380, 2000.
- Molnar, P., and H. Lyon-Caen, Some simple physical aspects of the support, structure, and evolution of mountain belts, in *Processes in Continental Lithospheric Deformation*, edited by S. P. Clark Jr., B. C. Burchfiel, and J. Suppe, *Spec. Pap. Geol. Soc. Am.*, 218, 179–207, 1988.
- Molnar, P., and P. Tapponnier, Cenozoic tectonics of Asia: Effects of a continental collision, *Science*, 189, 419–426, 1975.
- Molnar, P., E. T. Brown, B. C. Burchfiel, Q. Deng, X. Feng, J. Li, G. M. Raisbeck, J. Shi, Z. Wu, F. Yiou, and H. You, Quaternary climate change and the formation of river terraces across growing anticlines on the north flank of the Tien Shan, China, *J. Geol.*, 102, 583–602, 1994.
- Mugnier, J. L., S. Guellec, G. Menard, F. Roure, M. Tardy, and P. Viallon, A crustal scale balanced cross-section through the external Alps deduced from the ECORS profile, in *Deep Structure of the Alps*, edited by F. Roure, P. Heitzmann, and R. Polino, pp. 203–216, Soc. Geol. de Fr., Paris, 1990.
- Narr, W., and J. Suppe, Kinematics of basement-involved compressive structures, *Am. J. Sci.*, 294, 802–860, 1994.
- Nelson, K. D., et al., Partially molten middle crust beneath southern Tibet: Synthesis of Project INDEPTH results, *Science*, 274, 1684–1688, 1996.
- Nelson, M. R., R. McCaffrey, and P. Molnar, Source parameters for 11 earthquakes in the Tien Shan, central Asia, determined by  $P$  and  $SH$  waveform inversion, *J. Geophys. Res.*, 92, 12,629–12,648, 1987.
- Ni, J., Contemporary tectonics in the Tien Shan region, *Earth Planet. Sci. Lett.*, 41, 347–354, 1978.
- Ollerhead, J., D. J. Huntley, and G. W. Berger, Luminescence dating of the Buctouche Spit, New Brunswick, *Can. J. Earth Sci.*, 31, 523–531, 1994.
- Prescott, J. R., and J. T. Hutton, Cosmic ray and gamma ray dosimetry for TL and ESR, *Nucl. Tracks Radiat. Meas.*, 14, 223–227, 1988.
- Ramsey, B. C., Radiocarbon calibration and analysis of stratigraphy: The OxCal Program, *Radiocarbon*, 37(2), 425–430, 1995.
- Ramsey, C. B., Probability and dating, *Radiocarbon*, 40(1), 461–474, 1998.
- Rockwell, T. K., E. A. Keller, and G. R. Dembroff, Quaternary rate of folding of the Ventura Avenue Anticline, western Transverse Ranges, southern California, *Geol. Soc. Am. Bull.*, 100, 850–858, 1988.
- Rodgers, J., Chains of basement uplifts within cratons marginal to orogenic belts, *Am. J. Sci.*, 287, 661–692, 1987.
- Rubin, C. M., S. Thompson, K. Abdrakhmatov, and R. Weldon, Thrust fault paleoseismology in an intercontinental tectonic setting, Kyrgyz Tien Shan, central Asia, *Geol. Soc. Am. Abstr. Programs*, 31(7), 376, 1999.
- Sadybakasov, I., *Neotectonics of the Central Tien Shan* (in Russian), 117 pp., Ilim, Bishkek, Kyrgyzstan, 1972.
- Sadybakasov, I., *Neotectonics of High Asia* (in Russian), 176 pp., Nauka, Moscow, 1990.
- Schulz, S. S., *Analysis of the neotectonics and relief of the Tien Shan* (in Russian), 222 pp., Geografiz, Moscow, 1948.
- Shackleton, N. J., The 100,000-year ice-age cycle identified and found to lag temperature, carbon dioxide, and orbital eccentricity, *Science*, 289, 1897–1902, 2000.
- Shirokova, Y. I., A detailed study of the stresses and faults at earthquake foci of central Asia, *Izv. Acad. Sci. USSR Phys. Solid Earth*, 11, 707–717, 1974.
- Sieh, K. E., and R. H. Jahns, Holocene activity of the San Andreas fault at Wallace Creek, California, *Geol. Soc. Am. Bull.*, 95, 883–896, 1984.
- Stuiver, M., and H. A. Polach, Discussion; reporting of C-14 data, *Radiocarbon*, 19(3), 355–363, 1977.
- Stuiver, M., and P. J. Reimer, A computer program for radiocarbon age calibration, *Radiocarbon*, 28(2B), 1022–1030, 1986.
- Stuiver, M., P. J. Reimer, E. Bard, J. W. Beck, G. S. Burr, K. A. Hughen, B. Kromer, G. McCormac, J. van der Plicht, and M. Spurk, INTCAL98 radiocarbon age calibration, 24,000–0 cal BP, *Radiocarbon*, 40(3), 1041–1083, 1998.
- Suppe, J., Geometry and kinematics of fault-bend folding, *Am. J. Sci.*, 283, 684–721, 1983.
- Suppe, J., and D. A. Medwedeff, Geometry and kinematics of fault-propagation folding, *Eclogae Geol. Helv.*, 83(3), 409–454, 1990.
- Tapponnier, P., and P. Molnar, Active faulting and Cenozoic tectonics of the Tien Shan, Mongolia, and Baykal regions, *J. Geophys. Res.*, 84, 3425–3459, 1979.
- Tarasov, S. A., *Cenozoic Geology and Neotectonics of the Tien Shan* (in Russian), 211 pp., Ilim, Bishkek, Kyrgyzstan, 1970.
- Thompson, S. C., Active Tectonics in the central Tien Shan, Kyrgyz Republic, Ph.D. thesis, Univ. of Wash., Seattle, 2001.
- Thompson, S. C., R. J. I. Weldon, C. M. Rubin, and K. Y. Abdrakhmatov, Late Quaternary river terraces provide kinematic tests for fault-related folding in the Kyrgyz Tien Shan, central Asia, *Geol. Soc. Am. Abstr. Programs*, 31(7), 128, 1999.
- Trifonov, V. G., V. I. Makarov, and V. F. Skobelev, The Talaso-Fergana active right-slip fault, *Geotectonics*, 24(5), 435–444, 1991.
- Ward, G. K., and S. R. Wilson, Procedures for comparing and combining

- radiocarbon age determinations: A critique, *Archaeometry*, 20(1), 19–31, 1978.
- Weldon, R. J., Late Cenozoic geology of Cajon Pass: Implications for tectonics and sedimentation along the San Andreas Fault, Ph.D. thesis, Calif. Inst. of Technol., Pasadena, 1986.
- Weldon, R. J. I., and K. E. Sieh, Holocene rate of slip and tentative recurrence interval for large earthquakes on the San Andreas Fault, Cajon Pass, southern California, *Geol. Soc. Am. Bull.*, 96, 793–812, 1985.
- Willett, S. D., Dynamic and kinematic growth and change of a Coulomb wedge, in *Thrust Tectonics*, edited by K. R. McClay, pp. 19–31, Chapman and Hall, New York, 1992.
- Willett, S. D., Rheological dependence of extension in wedge models of convergent orogens, *Tectonophysics*, 305, 419–435, 1999.
- Yeats, R. S., and R. J. Lillie, Contemporary tectonics of the Himalayan frontal fault system: Folds, blind thrusts and the 1905 Kangra earthquake, *J. Struct. Geol.*, 13, 215–225, 1991.
- Yin, A., S. Nie, P. Craig, T. M. Harrison, F. J. Ryerson, X. Qian, and G. Yang, Late Cenozoic tectonic evolution of the southern Chinese Tien Shan, *Tectonics*, 17, 1–27, 1998.
- 
- K. Abdrakhmatov, Academy of Science, Kyrgyz Institute of Seismology, Asanbay 52/1, Bishkek 720060, Kyrgyzstan.
- G. W. Berger, Earth and Ecosystems Science, Desert Research Institute, 2215 Raggio Pkwy., Reno, NV 89512-1095, USA. (gwberger@dri.edu)
- P. Molnar, University of Colorado at Boulder, Department of Geological Sciences, Boulder, CO 80309, USA. (peter.molnar@colorado.edu)
- C. M. Rubin, Central Washington University, Department of Geological Sciences, Lind Hall, Ellensburg, WA 98926, USA. (charlier@cwu.edu)
- S. C. Thompson and R. J. Weldon, Department of Geological Sciences, University of Oregon, Eugene, OR 97403-1272, USA. (stevet@u.washington.edu; ray@newberry.uoregon.edu)